Dynamic Control of Chromatin-associated m^{6}A Methylation Regulates Nascent RNA Synthesis

Wenqi Xu[1, #], Chenxi He[1, #], Emily G. Kaye[2], Jiahui Li[1], Mandi Mu[1], Geoffrey M. Nelson[2], Li Dong[1], Jiahua Wang[1], Feizhen Wu[1], Yujiang Geno Shi[3], Karen Adelman[2, *], Fei Lan[1, *], Yang Shi[4, *] and Hongjie Shen[1, 5 *]

[1] Center for Medical Research and Innovation, Shanghai Pudong Hospital, Fudan University Pudong Medical Center, the Shanghai Key Laboratory of Medical Epigenetics, the International Co-laboratory of Medical Epigenetics and Metabolism, Ministry of Science and Technology, Institutes of Biomedical Sciences, Fudan University, Shanghai 201399, China.

[2] Department of Biological Chemistry and Molecular Pharmacology, Blavatnik Institute, Harvard Medical School, Boston, MA 02115, USA

[3] Division of Endocrinology, Diabetes and Hypertension, Department of Medicine, Brigham and Women's Hospital, Harvard Medical School, Boston, MA 02115, USA.

[4] Ludwig Institute for Cancer Research, Oxford Branch, Oxford University, Oxford OX3 7DQ, UK

[5] Lead Contact

[#] Equally contribution

* Correspondence:
yang.shi@ludwig.ox.ac.uk (Y.S.)
hongjieshen@fudan.edu.cn (H.S.)
fei_lan@fudan.edu.cn (F.L.)
karen_adelman@hms.harvard.edu (K.A.)

SUMMARY

N^6-methyladenosine (m^{6}A) regulates various aspects of RNA biology. Although m^{6}A methylation on mRNA has been shown to be co-transcriptionally deposited, a possible regulatory role of m^{6}A on transcription remains poorly understood. Here, we demonstrate that the METTL3/METTL14/WTAP m^{6}A methyltransferase complex (MTC) components are co-localized to many promoters and enhancers and deposit the m^{6}A modification to local chromatin associated transcripts including pre-mRNAs, promoter upstream transcripts (PROMPTs) and enhancer RNAs (eRNAs), suggesting a possible regulatory role for m^{6}A methylation at these transcripts. Indeed, PRO-seq analyses demonstrate that nascent RNAs originating from both promoters and enhancers are significantly decreased in the METTL3 depleted cells. Interestingly, we find that genes targeted by the Integrator complex for premature termination are depleted of METTL3, suggesting an antagonistic relationship between METTL3 and the Integrator complex. Consistently, we found an elevated level of INTS11 at promoters and enhancers upon loss of MTC or nuclear m^{6}A binders. Taken together, our findings suggest that MTC-mediated m^{6}A modification protects nascent RNAs from Integrator-mediated termination and promotes productive transcription, thus unraveling a novel layer of gene regulation imposed by RNA m^{6}A modification.

INTRODUCTION

mRNA m^6A modification is catalyzed by the METTL3/METTL14/WTAP methyltransferase complex (MTC) and has been demonstrated to play important roles in mRNA regulation (Shi et al., 2019). METTL3 is the catalytic component of the MTC while its heterodimeric partner METTL14 contributes to substrate RNA binding (Sledz and Jinek, 2016; Wang et al., 2016; Wang et al., 2016). WTAP, on the other hand, plays a recruitment role for METTL3/METTL14 (Ping et al., 2014). MTC installs methylation on a conserved sequence motif of "RRACH" (R represents A or G, and H represents A, C, or U), mainly near stop codons and 3'UTR in mRNA (Dominissini et al., 2012; Meyer et al., 2012). The m^6A methylation-dependent processes can be controlled dynamically, and the reversal of m^6A methylation on RNA is mediated by ALKBH5 (AlkB homolog 5) and FTO (Jia et al., 2011; Zheng et al., 2013).

Recently, METTL3 has also been shown in different cell types to be significantly enriched at DNA damage sites (Xiang et al., 2017), promoters (Akhtar et al., 2021; Barbieri et al., 2017; Xiao et al., 2019), 3' UTR (Knuckles et al., 2017) and retrotransposons (Xu et al., 2021), respectively. Consistently, m^6A methylation has been shown to be present on chromatin associated RNA transcripts, including pre-mRNAs, PROMPTs, eRNAs and transposon RNAs (Liu et al., 2020; Louloupi et al., 2018; Xiao et al., 2019; Xu et al., 2021).

Interestingly, unlike on mRNA, m^6A methylation on chromatin-associated RNA transcripts is not limited to the 3' ends (Chelmicki et al., 2021; Xu et al., 2021), suggesting a distinct regulatory role. Supporting this hypothesis, several recent studies have demonstrated that m^6A impacts the stability of the chromatin-associated RNAs and local histone modifications (Chelmicki et al., 2021; Liu et al., 2020; Liu et al., 2021; Xu et al., 2021). Furthermore, m^6A has recently been suggested to play a role in the release of paused RNA polymerase II (Pol II) into productive elongation in *Drosophila* (Akhtar et al., 2021); however, how this might occur mechanistically and whether this occurs in mammalian cells remains unknown.

In this study, we investigated the role of MTC in transcription by profiling transcriptionally-engaged Pol II at base-pair resolution in the presence or absence of METTL3. We showed that METTL3 depletion down-regulates nascent RNAs originating from both promoters and enhancers at the TSS (Transcription Start Site) proximal regions, where MTC is significantly enriched. Mechanistically, we provide evidence that loss of METTL3 renders paused Pol II susceptible to the Integrator complex, which has been shown to attenuate transcription through pre-mature termination of nascent RNAs (Elrod et al., 2019). Collectively, our findings suggest a model where METTL3/14 catalyzed m^6A methylation on RNAs emanating from promoters and enhancers prevents premature cleavage of nascent transcripts mediated by the Integrator complex,

possibly by recruiting m^6A readers/binders to antagonize binding of the Integrator complex to these RNAs.

RESULTS

Genome-wide co-occurrence of the MTC components

To investigate the role of the chromatin-bound MTC, we first interrogated the chromatin binding patterns of its main components, i.e., METTL3, METTL14 and WTAP, in the human breast cancer cell line, MCF-7. We identified 5,578, 16,992 and 2,015 peaks of METTL3, METTL14 and WTAP, respectively. Most METTL3 peaks overlap with those of METTL14 (80.4%, 4,485/5,578, p value < 2.2e-16, Fisher's Exact Test) (Figure 1A), consistent with the notion that METTL3 and METTL14 form a heterodimer to mediate m^6A methylation (Sledz and Jinek, 2016; Wang et al., 2016; Wang et al., 2016). Compared with METTL3, fewer binding sites of WTAP were identified (2,015), consistent with the public PAR-CLIP data (WTAP, 752 and METTL3, 3,347 peaks, respectively) (Ping et al., 2014). Regardless, we found a substantial overlap of WTAP binding sites with those of METTL3 (34.7%, 699/2,015, p value < 2.2e-16, Fisher's Exact Test) or METTL14 (53.5%, 1,078/2,015, p value < 2.2e-16, Fisher's Exact Test) (Figure 1A). We also identified strong correlations of binding intensities among these three proteins over 1kb bins across the genome (Figure S1A). This finding is confirmed by ChIP-seq analysis of HEK293T cells expressing either HA-tagged METTL3, METTL14 or WTAP (12,108, 7,737 and 2,314 peaks of HA-METTL3, HA-METTL14 and HA-WTAP, respectively) (Figure S1B), where we again found significant overlaps of these three proteins (Figure S1C, p values < 2.2e-16, Fisher's Exact Test). Finally, we observed strong overlap

among the binding events of these three MTC components in mouse neural stem cells (mNSCs), in which 7,200 METTL3, 20,772 METTL14 and 2,480 WTAP peaks were identified, respectively (Figure S1D, p values < 2.2e-16, Fisher's Exact Test). These findings suggest that co-binding of the MTC components to chromatin regions is likely a shared feature in different cell types.

The mRNA m^{6}A MTC components bind promoters and enhancers

Consistent with previous studies indicating that METTL3 is significantly enriched at DNA damage sites (Xiang et al., 2017) and on promoters (Akhtar et al., 2021; Barbieri et al., 2017; Xiao et al., 2019), large subsets of peaks of METTL3 (41.7%), METTL14 (46.6%) or WTAP (40.9%) localize to promoter regions in MCF-7 cells compared with random peaks (2.3%) (Figure 1B, p values < 2.2e-16, Pearson's Chi-squared test). These peaks are enriched for histone marks associated with active promoters, i.e., H3K4me3 and H3K27Ac, but not the heterochromatin mark, H3K9me3 (Gates et al., 2017) (Figure 1C). In addition to promoters, we also found substantial numbers of m^{6}A MTC peaks at introns and distal intergenic sites (Figure 1B). By sorting genes according to the distances between their TSS and the nearest METTL3 binding site, we found the TSS distal MTC peaks are associated with very weak H3K4me3 but relatively strong H3K4me1, H3K27Ac and p300 signals, suggesting these regions may be active enhancers (Gates et al., 2017) (Figure S1E). Indeed,

using our ChIP-seq data for H3K4me1 and H3K27Ac to define putative enhancers (N=6,197, see Methods), we found that METTL3, METTL14 and WTAP binding events were significantly enriched in these regions, representing 25.0% of METTL3 (1,397/5,578), 27.9% of METTL14 (4,739/16,992), and 19.0% of WTAP (382/2,015) total peaks, respectively (Figures 1D, S1F, p values < 2.2e-16, Pearson's Chi-squared test). Furthermore, we identified 319 super enhancers in MCF-7 cells (Figure S1G), which consist of multiple enhancers in close genomic proximity. These super-enhancers are significantly and strongly co-occupied by METTL3, METTL14 and WTAP (Figures 1E and S1H, p values < 1.3e-8, Fisher's Exact Test). Genome Browser tracks of representative promoters, enhancers and a super enhancer are shown in Figures 1F and 1G. Similar observations were made in HEK293T (Figures S2A-B) and mouse neural stem cells (mNSCs) (Figures S2C-D).

m^{6}A MTC catalyzes m^{6}A methylation on RNAs transcribed from promoters and enhancers

We next determined whether m^{6}A is deposited on chromatin associated transcripts near the MTC chromatin binding sites by carrying out MeRIP (Methylated RNA Immunoprecipitation) using chromatin associated ribo-depleted RNAs (Figure S3A). We discovered a total of 233,557 MeRIP peaks and among them 16,366 and 11,986 localize to promoters and enhancers,

respectively. De novo motif calling readily identified the presence of the known mRNA m^{6}A methylation consensus motif, RR(m^{6}A)CH (Dominissini et al., 2012; Meyer et al., 2012) (Figure S3B), indicating these peaks likely represent *bona fide* m^{6}A sites catalyzed by METTL3. Supporting this idea, we found a significant reduction of the MeRIP m^{6}A signals upon knockdown of METTL3 (Figures S3C-D).

To further investigate the distribution of m^{6}A on these transcripts, we first defined the active TSSs of pre-mRNAs, PROMPTs and eRNAs in MCF-7. Briefly, candidate TSSs obtained from the public CAGE-seq dataset (FANTOM5, see Methods) are filtered with PRO-seq densities (TPM>1 at TSS 0-100 bp regions) and adjacent TSSs within 100 bp are merged. Together, we defined TSS for 11,936 mRNA, 1,159 PROMPTs and 2,488 enhancer RNAs, respectively. We showed that m^{6}A signals are significantly enriched near the TSSs of these transcripts (Figures 2A-C), which is consistent with the ChIP-seq data showing enrichment of METTL3, METTL14 and WTAP at these regions, and suggests that chromatin-bound MTC catalyzes m^{6}A methylation of nascent RNAs at their 5' ends (Figures 2D-F). Supporting this hypothesis, we showed that the TSS proximal m^{6}A enrichment is significantly reduced in METTL3 KD cells, suggesting these regions are decorated by *bona fide* m^{6}A (Figures 2G-H). Although METTL3 depletion substantially reduces the MeRIP enrichment at TSS proximal regions, residual MeRIP signals are observed on some

transcripts, likely due to incomplete depletion of METTL3 protein, as well as the m^6Am modification mediated by PCIF1 (Akichika et al., 2019; Sendinc et al., 2019).

In order to determine whether chromatin RNA MeRIP-seq captured m^6A on nascent transcripts, we looked at the reads mapped to introns, which should be derived from pre-mRNAs rather than mature mRNAs. Consistent with a previous study (Ke et al., 2017), we found a significantly larger proportion of intronic reads in chromatin-associated RNA-seq (79.1%) than poly A RNAs-seq (33.3%, raw data: GSM5685633) (Figure S3E), and a significantly lower intron splicing efficiency of chromatin-associated RNAs than poly A RNAs (Figure S3F). We thus reasoned that intronic reads should be enriched in nascent RNA as suggested previously (Gaidatzis et al., 2015). Therefore, we extracted the MeRIP reads that mapped to introns. Using these intronic reads only, we detected significant m^6A enrichment over input, supporting that m^6A is incorporated into pre-mRNAs (Figure S3G).

The m^6A MTC positively regulates the synthesis of PROMPT and eRNA transcripts

Though the regulatory role of the m^6A modification at 3' UTRs and stop codons of mRNAs has been well-established, the function of the same modification at

the 5’ ends of RNAs remains incompletely understood. Interestingly, recent studies in *Drosophila*, in which METTL3-dependent m^{6}A is mostly enriched at the 5’ UTRs of genes, shows that m^{6}A within 5’ UTRs has no impact on RNA stability (Kan et al., 2021; Wang et al., 2021), suggesting that m^{6}A at 5’ UTRs may play a distinct role from the well-known function of m^{6}A at 3’ UTRs of mRNAs.

To determine whether and how the 5’ end-enriched m^{6}A regulates transcripts emanating from promoters and enhancers, we carried out Precision Run-on (PRO)-seq in control and METTL3 KD cells. This assay of nascent RNA measures instantaneous transcription activity, rather than steady state RNAs, allowing us to probe a role for m^{6}A on the process of transcription. Consistent with previous studies (Core and Adelman, 2019), we observed a significant TSS proximal enrichment of PRO-seq signals at mRNA TSSs, indicative of RNA Pol II pausing (Figure 3A). We further showed that METTL3 KD caused a significant decrease of averaged PRO-seq signals at the promoter proximal peak (Figures 3A-C, S3D), indicating that the amount of paused Pol II is reduced upon METTL3 depletion. We also observed similar changes at the TSSs of PROMPTs and eRNAs (Figures 3D-I). These changes were further confirmed by RT-qPCR analyses of four representative transcripts (Figure S3H).

We next wished to determine whether these changes are directly regulated by METTL3 bound to local TSSs by comparing the nascent RNA fold changes at TSSs with the high and the low METTL3 binding, respectively. In order to reduce the bias caused by the difference of basic expression level, we determined expression-matched TSSs (n=500) from METTL3 high binding TSSs (top 40%) and METTL3 low binding TSSs (bottom 60%), respectively (Figures S3F and S3I). We observed a substantially greater reduction of PRO-seq signals at the “METTL3 high” TSSs than the “METTL3 low” ones (Figure 3J). We observed similar correlations for PROMPTs and eRNAs where TSSs with higher densities of METTL3 are correlated with a greater reduction of PRO-seq signals upon METTL3 KD (Figures 3K-L, S3J-K, S3M-N).

The marked drop in PRO-seq signal near TSSs in METTL3-depleted cells suggested that the loss of METTL3 could be enabling promoter-proximal termination. TSS proximal termination is typically mediated by the endonuclease activity of the Integrator complex (Elrod et al., 2019). In order to determine whether METTL3 regulates nascent RNA termination through the Integrator complex, we carried out PRO-seq in cells depleted of INTS11, the endonuclease subunit of the Integrator complex, or cells depleted of both INTS11 and METTL3 (Figure S4A). Importantly, when compared with the INTS11 KD cells, the INTS11/METTL3 double KD cells showed no decrease of the TSS proximal nascent RNAs, suggesting that METTL3 can promote

transcription by antagonizing INTS11 (Figures 3M-O, S4B-D). Interestingly, the level of the PRO-seq signals in the double KD cells is even higher than that in the INTS11 KD cells, suggesting that METTL3 may promote transcription of its target genes via mechanisms besides antagonizing Integrator activity (Figures 3M-O, S4B-D).

PROMPTs and eRNAs are negatively regulated by chromatin bound m^{6}A demethylase ALKBH5

ALKBH5 has been reported to be a mRNA m^{6}A demethylase (Zheng et al., 2013). In order to investigate whether it also plays a role in regulating the abundance of RNAs generated at promoters and enhancers, we first asked whether ALKBH5 is associated with the same genomic regions as the m^{6}A MTC. We expressed HA-tagged ALKBH5 in MCF-7 cells and carried out ChIP-Seq using an HA antibody. We identified 9,453 ALKBH5 peaks and 33.3% of them (3,149) overlapped with those of METTL3 (Figure 4A, p value < 2.2e-16, Fisher's Exact Test). Similarly, we also identified a significant percentage of ALKBH5 overlapping with METTL3 signals in HEK293T cells (64.2%) (Figures S4E-F, p values < 2.2e-16, Fisher's Exact Test) and in mNSCs (84.8%) (Figures S4E, and S4G, p values < 2.2e-16, Fisher's Exact Test). We found ALKBH5 enrichment at promoters and enhancers, and this enrichment pattern overlaps that of MTC (Figures 4B-C), suggesting that nascent RNAs may be dynamically

regulated by both the m^{6}A methyltransferase and the demethylase. Similar results were found in HEK293T and mNSCs cells (Figures S4H-K). Further supporting this hypothesis, overexpression of ALKBH5 reduced the nascent RNA levels from these regions in MCF-7 (Figure 4D). Taken together, we conclude that the m^{6}A modification in nascent mRNAs, PROMPTs and eRNAs is subjected to regulation by the chromatin-associated MTC methylase complex and the demethylase ALKBH5, and that the m^{6}A is likely to be involved in the regulation of nascent RNA synthesis.

Loss of m^{6}A promotes INTS11 recruitment, which mediates nascent RNA cleavage

We next investigated the mechanism underlying the functional antagonism between METTL3 and the Integrator complex discussed above. We carried out ChIP-seq of INTS11 in the METTL3 KD, METTL14 KD and WTAP KD cells as well as control cells. We found a significant increase of the INTS11 enrichment level upon depletion of METTL3, METTL14 or WTAP, suggesting that MTC impaired INTS11 binding (Figures 5A-F). In addition, we observed a greater increase of INTS11 binding at the “METTL3 high” TSSs than the “METTL3 low” TSSs in the METTL3 depleted cells, suggesting that INTS11 binding is likely to be regulated through TSSs bound METTL3 (Figures 5G-I).

We next asked whether a similar antagonistic relationship between MTC and Integrator exists in other organisms. Consistent with Integrator-mediated termination, previous studies in *Drosophila* S2 cells showed that Integrator is enriched at genes with unstable pausing and fast decay of promoter Pol II (Figure 6A, Elrod et al., 2019). Interestingly, METTL3 ChIP-seq in S2 cells revealed that METTL3 is depleted at Integrator target genes, and enriched at genes with more stable Pol II binding (Figures 6B-D). Consistent with this, we found that the overlap of METTL3 highly bound genes (top 10%, n=839) and Integrator highly bound genes (top 10%, n=839) is very small (n=45) (Figure S5A). These findings suggest that METTL3 activity may stabilize Pol II against Integrator-mediated termination. To evaluate this, we carried out PRO-seq in S2 cells depleted of the Integrator subunit IntS9, as compared to mock depleted cells (Figure S5B). Comparison of the top 500 METLL3 bound genes with 500 expression matched controls (from the lower 50% of METTL3 occupancy) shows that genes highly bound by METTL3 are less affected by Integrator loss (Figure 6E). Together, these data suggest that METTL3 targets have more stably paused Pol II because they are protected from Integrator-mediated termination. Interestingly, whereas both METTL3 and Integrator bind paused RNAPII and positively correlate with promoter PRO-seq levels, the relationship between METTL3 and IntS1 signal at promoters is weakly negative (Spearman's correlation coefficient, r=-0.12, Figure S5C), suggesting that these factors are recruited by distinct signals. Consistent with this, a recent study

reported that the Integrator complex interacts with the histone methyltransferase complex PRC2 (Zhang et al., 2021), suggesting an additional crosstalk between histone modifications and Integrator binding.

m^{6}A binders are involved in the METTL3-Integrator antagonistic regulation

To further explore the molecular mechanism of the decrease of nascent RNA levels in the absence of MTC, we hypothesized that a factor may be involved in protecting the m^{6}A modified nascent RNAs from being recognized and processed by INTS11. This hypothesis would predict that such a factor should have the ability to co-transcriptionally recognize m^{6}A on the nascent RNAs, and upon its loss, nascent RNAs would be subjected to cleavage even in the presence of the m^{6}A modification. Recent studies demonstrate that m^{6}A methylation exposes the surrounding sequences, which allow binding of the hnRNP G protein (Liu et al., 2017). Importantly, hnRNP G has also been shown to function co-transcriptionally with Pol II (Liu et al., 2017; Zhou et al., 2019), thus prompting us to investigate whether hnRNP G is involved in m^{6}A-mediated nascent RNA regulation. Consistent with our hypothesis, through Cut &Tag-seq (Kaya-Okur et al., 2019) or ChIP-seq, we found hnRNP G binds to promoters and enhancers (Figures 7A-B). Importantly, INTS11 chromatin association was significantly enhanced upon loss of hnRNP G (Figures 7C, S5D), which was accompanied by a significantly reduced level of nascent RNAs (Figure 7D),

similarly to what happened upon m^{6}A MTC knockdown. Interestingly, we found the nuclear m^{6}A reader, YTHDC1, interacts with hnRNP G (Figure S5E), suggesting that hnRNP G and YTHDC1 may both regulate nascent RNA levels. Consistently, we found reduction of PROMPTs and eRNAs upon knockdown of YTHDC1 but not the cytosolic m^{6}A reader, YTHDF2 (Figures S5F-G).

Taken together, our findings demonstrate that the m^{6}A MTC and ALKBH5 are associated with promoters and enhancers where they regulate nascent RNA abundance through m^{6}A methylation. Mechanistically, m^{6}A modified nascent RNAs are protected by hnRNP G and possibly YTHDC1 from INTS11-mediated premature termination (Figure 7E), thus promoting productive transcription.

DISCUSSION

RNA m^{6}A methylation is extensively studied as a mechanism that regulates mRNA stability post-transcriptionally. However, m^{6}A is co-transcriptionally deposited onto nascent RNAs (Ke et al., 2017), raising the question of whether and how it regulates the transcription process *per se*. This study investigated the chromatin-bound m^{6}A regulators and provided evidence supporting the model where dynamic regulation of nascent RNA m^{6}A methylation impacts the nascent RNA synthesis. This conclusion is supported by multiple lines of evidence including the demonstrations that 1) the m^{6}A methyltransferase complex mediates m^{6}A methylation on nascent RNAs derived from both promoters and enhancers, and this process is likely to be regulated by the demethylase ALKBH5 as well; 2) m^{6}A on these nascent RNAs is recognized by nuclear m^{6}A binding proteins; 3) m^{6}A methylation and recognition are important to impede the action of the Integrator complex, which would otherwise access and cleave the nascent RNAs, leading to premature transcriptional termination; 4) the proposed antagonistic relationship between METTL3 and Integrator appears to be conserved from invertebrates (*Drosophila*) to vertebrates (human cells).

A recent study suggests that termination of non-productive, stalled Pol II by Integrator complex may help to recycle the Pol II apparatus for the elongation

of ‘productive’ RNAs (Lykke-Andersen et al., 2021). An interesting question that remains is how the Integrator complex distinguishes which elongation complexes to target for termination (Lykke-Andersen et al., 2021). Importantly, our study suggests that m^6A modification may be such a signal for the Integrator complex to distinguish between “non-productive” and “productive” RNAs.

Mechanistically, we demonstrated that METTL3 negatively regulated TSS proximal premature transcription termination by impairing the recruitment of the integrator complex, which suggests that m6A RNA modification can facilitate nascent RNA synthesis. Interestingly, a recent study shows that MTC recruitment to gene promoters is dependent on transcription (Akhtar et al., 2021). Specifically, depletion of transcription elongation factor SPT6 significantly compromised METTL3 binding at promoters, suggesting that active transcription elongation facilitates METTL3 binding. Together, these studies suggest a positive feedback mechanism where METTL3 prevents premature termination to allow for elongation, which in turn promotes METTL3 recruitment.

We note that the magnitude of the antagonism between METTL3 and Integrator may not fully explain the ability of METTL3 to positively regulate transcription. Thus, m^6A deposited by METTL3 at nascent RNAs might also play other

regulatory roles, transcriptionally and/or post-transcriptionally. In this context, it's interesting to note that a recent study shows that m^{6}A on eRNAs regulates downstream gene transcription by promoting the formation of m^{6}A-eRNA/YTHDC1 condensate, which co-mixes with and facilitates the formation of BRD4 coactivator condensates (Lee et al., 2021).

In summary, our findings elucidated a novel, evolutionarily conserved role for RNA m^{6}A methylation in promoting transcription by antagonizing premature transcriptional termination driven by the Integrator complex. These findings suggest a protective role of m^{6}A in nascent RNA synthesis on chromatin, which contrasts with a disruptive role of m^{6}A in promoting mRNA degradation in cytosol (Lasman et al., 2020; Zaccara and Jaffrey, 2020), suggesting that m^{6}A may differentially impact RNAs at different stages of their life cycles, or RNAs in different subcellular locations. Additionally, a recent study found that in mES (J-1) cells, m^{6}A methylation of the chromatin associated regulatory RNAs (CarRNAs), which include PROMPTs and eRNA, as well as LINE-1 repeat RNAs, appears to negatively regulate their stability (Liu et al., 2020). However, another study using a different mESC line (E14) reported that LINE1 RNA levels remain globally unaffected or even down-regulated upon KO of Mettl3 or other MTC components (Chelmicki et al., 2021). These recent findings, together with ours, further highlight the complexed nature of m^{6}A-mediated regulation of RNA fate.

ACKNOWLEDGEMENTS

H.S. was sponsored by National Key R&D Program of China (2021YFA1102200, 2021YFA1301700), Shanghai Rising-Star Program (19QA1401300) and National Science Foundation of China (81874157, 32070649, 32122020). W.X. was sponsored by National Science Foundation of China (31900469) and China Postdoctoral Science Foundation (2020T130116, 2019M661350). Support was also provided by NIH R01GM134539 to K.A. Y.S. is an American Cancer Society Research Professor.

AUTHOR CONTRIBUTIONS

W.X. carried out the bioinformatics analyses described in this manuscript for mammalian cells. H.S. and C.H. carried out most of the experiments. J.L. and L.D. provided discussions on Cut&Tag. M.M. and J.W. carried out some of the Western blotting experiments. F.W. provided discussion and advice on bioinformatics analyses. E.G.K performed *Drosophila* PRO-seq and Western blotting, and bioinformatic analyses in Figure 6, under the supervision of K.A. G.N and K. A. provided discussion and advice on PRO-seq and data analysis. W.X, H.S., F.L. and Y.S. conceived the project with input from Y.G.S. W.X, H.S. and Y.S. directed all the experiments and co-wrote the manuscript.

DECLARATION OF INTERESTS

Y.S. is a co-founder of and holds equity in K36 Therapeutics, Inc, Y.S. also holds equity in Imago Biosciences, Inc. Y.S. is a consultant for Active Motif, Inc, a member of the Scientific Advisory Board of the College of Life Sciences, West Lake University, and a member of the MD Anderson External Advisory Board. K.A. received research funding from Novartis not related to this work, is a consultant for Syros Pharmaceuticals, is on the SAB of CAMP4 Therapeutics, and is a member of the Advisory Board of Molecular Cell. All other authors declare no competing interests.

Figure1: The m^{6}A MTC components bind promoters and enhancers in MCF-7 cells

A. Venn diagram showing overlap of ChIP-seq peaks of METTL3, METTL14 and WTAP.

B. Bar plots showing the peaks distribution of METTL3, METTL14 and WTAP.

C-D. Heatmaps showing the enrichments (ChIP relative to Input) of METTL3, METTL14, WTAP and different histone modifications over promoters (H3K4me3 and H3K27Ac) (C) and enhancers (H3K4me1 and H3K27Ac) (D). Heatmaps were ranked by METTL3 enrichment.

E. Aggregation plots showing the binding patterns of METTL3 (Top), METTL14 (Middle) and WTAP (Bottom) over super enhancers.

F-G. Snapshots of UCSC genome browser showing METTL3, METTL14 and WTAP binding events at three representative promoters (F), and three representative typical enhancers and one super enhancer (G).

For ChIP-seq, representative of two biological replicates were shown. Pearson correlation coefficients for the biological replicates are listed in Table S3.

Figure 2: The m^{6}A MTC catalyzes m^{6}A in mRNAs, PROMPTs and eRNAs

A-C. Aggregation plots showing m^{6}A enrichment over mRNA TSS (A) and PROMPT TSS (B) and eRNA TSS (C) in MCF-7 cells.

D-F. Heatmaps showing METTL3, METTL14, WTAP enrichment over mRNA TSS (D) and PROMPT TSS (E) and eRNA TSS (F) in MCF-7 cells.

G. Boxplots showing m^{6}A enrichment (IP/Input) over m^{6}A peaks localized to TSS to TSS+100 region of mRNA (Left), PROMPT (Middle) and eRNA (Right) in control and METTL3 KD MCF-7 cells. m^{6}A signal at m^{6}A peaks was calculated and Paired t-test was used.

H. Snapshots of UCSC genome browser showing m^{6}A enrichment (IP/Input) over mRNA TSSs (Left), PROMPT TSSs (Middle) and eRNA TSSs (Right) in control and METTL3 KD MCF-7 cells.

For MeRIP-seq and ChIP-seq, representative of two biological replicates were shown. Pearson correlation coefficients for the biological replicates are listed in Table S3.

Figure 3: The m^{6}A MTC regulates nascent RNA biogenesis

A-C. Aggregation plots (A), Snapshots of UCSC genome browser (B) and Boxplots (C) showing the nascent RNA level decreases upon METTL3 KD over Pre-mRNAs in MCF-7 cells. PRO-seq signal at TSS to TSS+100 region was calculated and Paired t-test was used for in C.

D-F. Aggregation plots (D), Snapshots of UCSC genome browser (E) and Boxplots (F) showing the nascent RNA level decreases upon METTL3 KD over PROMPTs in MCF-7 cells. PRO-seq signal at TSS to TSS+100 region was calculated and Paired t-test was used for in F.

G-I. Aggregation plots (G), Snapshots of UCSC genome browser (H) and Boxplots (I) showing the nascent RNA level decreases upon METTL3 KD over eRNAs in MCF-7 cells. PRO-seq signal at TSS to TSS+100 region was calculated and Paired t-test was used for in I.

J-L. Aggregation plots showing the nascent RNA level change upon METTL3 KD over ”METTL3 high” and “METTL3 low” mRNA TSSs (n=500) (J), PROMPT TSSs (n=200) (K), eRNA TSSs (n=200) (L) in MCF-7 cells.

M-O. Boxplots showing nascent RNA changes after individual or combined siRNA treatment for METTL3 and INTS11 over mRNA TSSs (M), PROMPT TSSs (N) and eRNA TSSs (O) in MCF-7 cells. PRO-seq signal at TSS to TSS+100 region was calculated and Paired t-test was used.

PRO-seq was carried out with spike-in *Drosophila* cells and normalized with reads mapped to the spike-in genome. For PRO-seq, representative of two biological replicates were shown. Pearson correlation coefficients for the biological replicates are listed in Table S3.

Figure 4: Nascent RNAs on promoters and enhancers are dynamically regulated by m^{6}A demethylase ALKBH5 in MCF-7 cells

A. Venn diagram showing overlap of ChIP-seq peaks between HA-ALKBH5 and METTL3 in MCF-7 cells.

B. Aggregation plots showing the HA-ALKBH5 binding levels over METTL3 bound promoters (Left) and enhancers (Right) in MCF-7 cells.

C. Snapshots of UCSC genome browser showing METTL3 and HA-ALKBH5 binding at two representative promoters (Left) and two representative enhancers (Right).

D. RT-qPCR assays showing nascent RNA level decreases upon ALKBH5 over-expression at two representative promoters and two representative enhancers.

For RT-qPCR, all data are represented as mean±SD from three biological repeats; ** p-value<0.01; t-test. For ChIP-seq, representative of two biological replicates were shown. Pearson correlation coefficients for the biological replicates are listed in Table S3.

Figure 5: Loss of m^{6}A promotes INTS11 recruitment, which mediates nascent RNA cleavage in MCF-7 cells

A-C. Aggregation plots showing the INTS11 binding level increases upon KD of METTL3, METTL14 or WTAP over mRNA TSS (A), PROMPT TSS (B), eRNA TSS (C) in MCF-7 cells.

D-F. Snapshots of UCSC genome browser showing the INTS11 binding level increases upon KD of METTL3, METTL14 or WTAP over mRNA TSS (D), PROMPT TSS (E), eRNA TSS (F) in MCF-7 cells.

G-I. Aggregation plots showing the INTS11 binding level change upon METTL3 KD over METTL3 high or low bound gene TSSs (n=500) (G), PROMPT TSSs (n=200) (H), eRNA TSSs (n=200) (I) in MCF-7 cells.

For ChIP-seq, representative of two biological replicates were shown.
Pearson correlation coefficients for the biological replicates are listed in Table S3.

Figure 6: METTL3 and Integrator bind to different sets of genes in *Drosophila*

A and B. Boxplots of the ChIP-seq signal (sum of reads TSS +/- 250) at each cluster of Pol II decay rates, defined in Elrod et al. (2019) for (A) IntS1 or (B) METTL3. Solid line represents median, with whiskers indicating 10th-90th percentiles. p-values are from Mann-whitney test.

C. Heatmap representations of ChIP-seq reads for METTL3 and IntS1 in S2 cells. Data are aligned around mRNA TSSs, shown as a green arrow (n=8389). Data are ranked by Promoter Pol II decay rate, where promoters with fastest decay rates (≤2.5 min) are on top. Dotted line separates each group of genes.

D. Average distribution of METTL3 ChIP-seq signal is shown, aligned around TSSs and divided into groups based on Pol II decay rate.

E. Average distribution of the difference in IntS9-depleted vs. Control PRO-seq signal at the top 500 METTL3-bound genes (red) versus expression-matched METTL3-low genes (blue).

PRO-seq was carried out with spike-in HEK293T cells and normalized with reads mapped to the spike-in genome. For PRO-seq, three biological repeats were combined. For ChIP-seq, two biological repeats were combined. Pearson correlation coefficients for the biological replicates are listed in Table S3.

Figure 7: m^{6}A protects nascent RNAs from INST11-mediated cleavage through hnRNP G

A. Aggregation plots showing hnRNP G binding (determined by Cut&Tag) over METTL3 bound promoters (Left) and enhancers (Right) in MCF-7 cells.

B. Snapshots of UCSC genome browser showing METTL3 and hnRNP G (Cut&Tag, and ChIP) binding at two representative promoters (Left) and two representative enhancers (Right) in MCF-7 cells.

C. Aggregation plots showing increase in INTS11 binding level over METTL3 bound promoters (Left) and enhancers (Right) upon KD of hnRNP G in MCF-7 cells.

D. RT-qPCR assays showing decrease in nascent RNA level upon hnRNP G KD at two representative promoters and two representative enhancers in MCF-7 cells.

E. Schematic model showing how m^{6}A MTC binds promoters and enhancers and protects local nascent RNAs from INTS11 dependent cleavage.

For RT-qPCR, all data are represented as mean±SD from three biological repeats; ** p-value<0.01; t-test. For ChIP-seq and Cut&Tag-seq, representative of two biological replicates were shown. Pearson correlation coefficients for the biological replicates are listed in Table S3.

STAR Methods

Resource Availability

Lead Contact

Further information and requests for resources and reagents may be directed to and will be fulfilled by the Lead Contact, Hongjie Shen (hongjieshen@fudan.edu.cn).

Materials Availability

All unique/stable reagents generated in this study are available from the Lead Contact with a completed Materials Transfer Agreement.

Data and Code Availability

The next-generation-sequencing data generated by this study have been deposited to GEO database under accession number GEO: GSE144404 and GSE186784.

Experimental Model and Subject Details

Cell culture

MCF-7, HEK293T were purchased from ATCC and cultured in DMEM (Hyclone, SH30243.01) supplemented with 10% fetal bovine serum (Gibco, 10091-148), 50 units/mL penicillin and 50 μg/mL streptomycin (Hyclone, SV30010). Mouse Neural Stem cells (mNSCs) were kindly provided by Dr. Jian Hu (MD Anderson Cancer Center) and cultured in NeuroCult NSC Basal Medium (Stemcell, 05702) supplemented with 20 ng/ml EGF (R&D, 236-EG), 20 ng/ml bFGF (Novoprotein, C779), 50 units/mL penicillin and 50 μg/mL streptomycin (Hyclone, SV30010).

Drosophila S2 cells (DGRC) were maintained at 26°C in Shields and Sang M3 insect media (Sigma S3652) supplemented with yeast extract (Sigma Y1000), bactopeptone (BD Biosciences 211677), and 10% fetal bovine serum (Thermo Fisher Scientific 16000, heat inactivated at 56°C).

Construction of stable cell lines and Knockdown

For construction of stable cell lines, retroviruses expressing plasmids (*METTL3, METTL14, WTAP or ALKBH5* were cloned into PMSCV) were produced by co-transfection of plasmids with Gag-Pol and Env in a 2:1:1 ratio into HEK293T cells using Lipofectamine 2000 (Invitrogen, 11668-019). Supernatant at 48 hour post-transfection was collected. HEK293T, MCF-7 or mouse neural stem cells were seeded in a 6-well plate and infected with each retroviruses in the presence of 5 μg/mL polybrene. Medium was replaced by fresh media with Puro (2 μg/ml) for 5 day, the surviving cells were pooled as stably infected cells.

For MCF-7 cells knockdown, SiRNAs were transfected using Lipofectamine RNAiMAX (Invitrogen, 13778-150). Cells were harvested after three days for Western blot and cell permeabilization. SiRNA oligonucleotides were listed at table S1.

For S2 cells knockdown, double-stranded RNAs to deplete IntS9 or control β-galactosidase (LacZ) were generated by in vitro transcription (MEGAscript kit, Thermo Fisher Scientific AMB13345) of PCR templates containing the T7 promoter sequence on both ends. Primer sequences were listed at table S1.

Knockdown experiments were performed in 25 cm^2 flasks using 5 x 10^6 cells with 25 μg dsRNA in 2.5 mL serum-free media in a 45 minute incubation. 2.5 mL media with 20% FBS was then added to achieve the standard 10% FBS cell culture conditions under which samples were incubated in for 3 days until harvesting for Western blot and cell permeabilization.

RT-qPCR

Total RNAs from cells were isolated using TRIzol reagent (Invitrogen, 15596018) and treated with TURBO DNase using TURBO DNA-free Kit (Invitrogen, AM1970) according to the manufacturer's instruction. cDNAs were synthesized with PrimeScript RT reagent kit (Takara, RR037A) containing random primers using 1μg of RNA per sample. RT-qPCR was performed using SYBR Premix ExTaq (Takara, RR420Q) with the Roche Lightcycler

480 Instrument II system. Primer sequences are listed in Table S2.

Western blots

1X SDS loading buffer was added to the samples directly and boiled for 10 min. The samples were loaded on SDS-PAGE gels and transferred from the gel to the membrane. Block the membrane for 1 h at room temperature using blocking buffer (5% milk in PBST). Incubate the membrane with appropriate dilutions (presented below) of primary antibody in blocking buffer overnight incubation at 4ºC. Wash the membrane in three washes of PBST, 5 min each. Incubate the membrane with the recommended dilution of conjugated secondary antibody in blocking buffer at room temperature for 1 h. Wash the membrane in three washes of PBST, 5 min each. For signal development, follow the kit manufacturer's recommendations and remove excess reagent. The intensity of the band was measured by Bio-Rad Image Lab software (Bio-rad). Primary antibodies concentrations used are as below: anti-METTL3 (1:3000, Bethyl); anti-METTL14 (1:3000, Sigma); anti-WTAP (1:3000, Bethyl); anti-ALKBH5 (1:1000, Abcam); anti-YTHDC1 (1:2000, CST); anti-YTHDF2 (1:2000, Proteintech); anti-dIntS9 (1:1000) (Ezzeddine et al., 2011), anti-H3 (1:1000 abcam ab1791), anti-Lamin B1 (1:5000, Proteintech); anti-ACTIN (1:5000, Proteintech); anti-GAPDH (1:5000, Proteintech).

Co-Immunoprecipitation

MCF-7 cells were washed once with PBS and lysed in lysis buffer (50 mM Tris pH7.5, 0.2% NP40, 1.5 mM $MgCl_2$, 10 mM KCl, 0.5 mM DTT, 10 mM Nethylmaleimide (NEM), 1mM PMSF and 1x Protease Inhibitor Cocktail) on ice for 15 min. The soluble fraction was collected by high speed centrifugation (13,000 rpm, 15 min, 4ºC) and incubated with indicated antibody or IgG for 6 hours at 4ºC, followed by the addition of Dynabeads protein A/G for another 2 hours. The beads were washed for 4 times with lysis buffer. 1X SDS buffer was directly added to the beads and boiled for 10 min. The samples were loaded on SDS-PAGE gels and subjected to immunoblotting using indicated antibodies.

Chromatin Immunoprecipitation (ChIP) and Seq

Cells were cross-linked by adding 1% formaldehyde directly to the media for 10 min at RT. Cross-linking was stopped by adding glycine to a final concentration of 0.125 M for 5 min at RT. The media was removed and the cells were washed twice with ice-cold PBS. The cells were then collected in ChIP lysis buffer (50 mM HEPES pH7.5, 500 mM NaCl, 1 mM EDTA, 1% Triton, 0.1% Na-deoxylcholate, 0.1% SDS) for sonication directly. ChIP samples were incubated with specific antibodies in the ChIP lysis buffer (50 mM HEPES pH7.5, 500 mM NaCl, 1 mM EDTA, 1% Triton, 0.1% Na-deoxylcholate, 0.1% SDS) overnight at 4ºC. The protein-DNA complexes were immobilized on protein A/G beads for another 2 hour. The bound fractions were washed 3 times with the lysis buffer, and 2 times with RIPA buffer (50 mM HEPES, 300 mM LiCl, 1 mM EDTA, 0.5% NP-40, 0.5% Na-deoxylcholate), and once with TE. Elution and reverse crosslinking were carried out in the elution buffer (50 mM Tris-HCl pH8.0, 10 mM EDTA, 1% SDS) 65ºC for 6 hours. After RNase A and Proteinase K digestion, DNA samples were purified using PCR extraction kit (QIAGEN, 28004). The purified DNA samples were used for library construction using ACCEL-NGS 2S PLUS DNA LIBRARY KIT (SWIFT, 21096) or VAHTS Universal Plus DNA Library Prep Kit for Illumina (Vazyme, ND617). Libraries were sequenced on Illumina instruments by Jiang Xi HaploX Biotechnology Co., LTD.

Cleavage Under Targets and Tagmentation (Cut&Tag) and Seq

For Cut&Tag-Seq, Hyperactive In-Situ ChIP Library Prep Kit for Illumina was performed following manufacturer's instructions (Vazyme, TD902).

PRO-Seq

PRO-Seq was carried as methods described (Elrod et al., 2019). Cells were washed once in ice-cold 1x PBS and re-suspended in Buffer W (10 mM Tris-HCl pH 8.0, 10% glycerol, 250 mM sucrose, 10 mM KCl, 5 mM $MgCl_2$, 0.5 mM DTT, protease in-hibitors cocktail (Roche), and 4 u/mL RNase inhibitor [SUPERaseIN, Ambion]) at the cell density of 10^7

cells/mL. 9x volume of Buffer P (10 mM Tris-HCl pH 8.0, 10% glycerol, 250 mM sucrose, 10 mM KCl, 5 mM $MgCl_2$, 0.5 mM DTT, 0.1% Igepal, protease in-hibitors cocktail (Roche), 4 u/mL RNase inhibitor [SUPERaseIN, Ambion]) was then immediately added. Cells were gently re-suspended and incubated for up to 5 min on ice. Cells were then recovered by centrifugation (800 x g for 4 min, or 1000 x g x 5 min for S2 cells) and washed in Buffer F (50 mM Tris-HCl pH 8.0, 40% glycerol, 5 mM $MgCl_2$, 0.5 mM DTT, 4 u/mL RNase inhibitor [SUPERaseIN, Ambion]). Washed permeabilized cells were finally re-suspended in Buffer F at a density of 10^6 cells/45 µL. For PRO-seq of S2 cells, permeabilized cells were spiked with 5 uL containing 5 x 10^4 permeabilized human HEK293T cells prior to run-on.

PRO-seq run-on reactions were carried out as follows: 10^6 permeabilized cells were added to the same volume of 2x Nuclear Run-On reaction mixture (10 mM Tris-HCl pH 8.0, 300 mM KCl, 1%Sarkosyl, 5 mM $MgCl_2$, 1 mM DTT, 200 mM biotin-11-A/C/G/UTP (Perkin-Elmer), 0.8 u/mL SUPERaseIN inhibitor [Ambion]) and incubated for 5 min at 37ºC and the reaction were stopped by Trizol. Permeabilized D*rosophila* S2 cells were performed for 5 min at 30ºC. For spike in of MCF-7 cells, *Drosophila* S2 and MCF-7 samples were mixed in a ratio of 1:4 for nascent RNA extraction. Nascent RNA was extracted using a Total RNA Purification Kit following the manufacturer's instructions (ZOME for MCF-7 cells, Norgen Biotek Corp. S2 cells).

For MCF-7 cells, extracted nascent RNA was fragmented by base hydrolysis in 0.25 N NaOH on ice for 10 min and neutralized by adding 1x volume of 1 M Tris-HCl pH 6.8. Fragmented nascent RNA was bound to 30 µL of Streptavidin M-280 magnetic beads (Thermo Fisher Scientific) in Binding Buffer (300 mM NaCl, 10 mM Tris-HCl pH 7.4, 0.1% Triton X-100). For S2 cells, an alternate protocol with chemical fragmentation was used. 100 µL nascent RNA was incubated for 30 sec at 65°C, then incubated on ice for 25 minutes. 100 µL 2X fragmentation buffer (150 mM Tris-HCl, pH 8.3, 225 mM KCl, and 9 mM $MgCl_2$) was added then samples were incubated at 94°C for 5 min followed by addition of 25 µL EDTA incubated on ice for 2 minutes. Fragmented nascent RNA was bound to 30

µL of DynaBeads MyOne Streptavidin C1 magnetic beads (Thermo Fisher Scientific) in Binding Buffer (300 mM NaCl, 10 mM Tris-HCl pH 7.4, 0.1% Triton X-100).

For either M-280 or C1 beads, samples were washed twice in High salt buffer (2 M NaCl, 50 mM Tris- HCl pH 7.4, 0.5% Triton X-100), twice in Binding buffer, and twice in Low salt buffer (5 mM Tris-HCl pH 7.4, 0.1% Triton X-100). Bound RNA was extracted from the beads using Trizol (Invitrogen) followed by ethanol precipitation.

For the first ligation reaction, fragmented nascent RNA was dissolved in H_2O and incubated with 10 pmol of reverse 30 RNA adaptor (5'p-rNrNrNrNrNrNrGrArUrCrGrUrCrGrGrArCrUrGrUrArGrArArCrUrCrUrGrArArC-/3'InvdT/) and T4 RNA ligase I (NEB) for 2 h at 20ºC. Ligated RNA was enriched with biotin-labeled products by another round of Streptavidin bead binding and washing (two washes each of High, Binding and Low salt buffers and one wash of 1x Thermo Pol Buffer (NEB)). To decap 5' ends, the RNA products were treated with RNA 5' Pyrophosphohydrolase (RppH, NEB) at 37 ºC for 30 min followed by one wash of High, Low and T4 PNK Buffer. To repair 5' ends, the RNA products were treated with Polynucleotide Kinase (PNK, NEB) at 37ºC for 30 min. 5' repaired RNA was ligated to reverse 5' RNA adaptor (5'-rCrCrUrUrGrGrCrArCrCrCrGrArGrArArUrUrCrCrA-3') with T4 RNA ligase I (NEB) for 2 h at 20ºC. Adaptor ligated nascent RNA was enriched with biotin-labeled products by another round of Streptavidin bead binding and washing (two washes each of High, Binding and Low salt buffers and one wash of 1x SuperScript IV Buffer [Thermo Fisher Scientific]), and reverse transcribed using 25 pmol RT primer (5'- AATGATACGGCGACCACC GAGATCTACACGTTCAGAGTTCTACAGTCCGA-3') for TRU-seq barcodes (RP1 primer, Illumina). A portion of the RT product was removed and used for trial amplifications to determine the optimal number of PCR cycles. For the final amplification, 12.5 pmol of RPI-index primers (for TRU-seq barcodes, Illumina) was added to the RT product with Phusion polymerase (NEB) under standard PCR conditions. Excess RT primer served as one primer of the pair used for the PCR. For MCF-7 cells the product was amplified 12-14

cycles and beads size selected (Vazyme) before being sequenced on an Illumina system. Need to note, during the last beads cleanup step, we added 2X volume DNA-clean beads to selectively discard the adaptor dimers (<150nt), and some fragments with very short insertions may also be discarded. It will be helpful to add 2.8X volume DNA-clean beads to capture all the fragments. For S2 cells the product was amplified for 9-10 cycles and size selected using ProNex Size-Selective Purification System (Promega). The final products were sequenced on NovaSeq in a paired end 60/50 bp cycle run.

Analyses of ChIP-seq and Cut&Tag-seq analysis

Raw reads were aligned to the hg19 or mm10 genome using Bowtie2 (v 2.2.5) (Langmead et al., 2009). PCR duplicates were removed using samtools (v1.7) (Li et al., 2009) rmdup. Genome coverage bedGraph files for UCSC genome browser were generated by deeptools (v 3.0.2) (Ramirez et al., 2016) bamCoverage with the parameters "-of bedgraph --normalizeUsing RPKM --binSize 5". Peaks were generated by macs2 (v 2.1.1.20160309) callpeak with parameters "-p 0.00001 --nomodel". Genome coverage bigwig files for heatmap and aggregation plot were generated by deeptools (v 3.0.2) bamCoverage with the parameter "--normalizeUsing RPKM --binSize 5". Heatmaps were generated by deeptools (v 3.0.2) computeMatrix and plotHeatmap. Aggregation plots were generated by deeptools (v 3.0.2) computeMatrix and plotProfile. Genome wide correlations among ChIP-seq libraries were carried out by deeptools (v 3.0.2) multiBigwigSummary. Genome distribution analyses of ChIP-seq peaks were carried out by R package ChIPseeker (3.10) (Yu et al., 2015). Promoters were defined as TSS-1kb to TSS+100bp. Typical enhancers were determined by H3K4me1 peaks overlapped with H3K27Ac peaks excluding promoters. Super enhancers were determined by ROSE algorithm (Loven et al., 2013).

Drosophila METTL3 ChIP-seq data from two replicates were combined using bedtools v2.27.1 unionbedg followed by adding the counts from each replicate (sum of columns 4 and 5). The sum of reads was calculated from -250 to +250 relative to the mRNA TSSs for each decay cluster defined above.

IntS1 ChIP-seq in DL1 cells was published previously (Elrod et al., 2019) and is available from GEO (GSE114467). Data was processed as published, using input subtracted values to get counts from -250 to +250 relative to the mRNA TSS. For the analysis in Figure 6A, count sums were then scaled to set the lowest value at 0. Box plots were generated using Prism v 9.2.0.

Analyses of PRO-seq

MCF-7 PRO-seq analysis was carried out as described (Judd et al., 2021). Briefly, paired-end reads were trimmed to remove adaptors and low-quality reads using fastp (0.21.0) (Chen et al., 2018). Trimmed reads mapping to rRNAs were excluded using bowtie2 (Langmead et al., 2009). The remaining reads were then aligned to dm6 (*Drosophila*) and hg19 (Homo Sapiens) genome assembly using bowtie2 (Langmead et al., 2009). Strand specific reads were separated by samtools (v1.7) (Li et al., 2009) view with specific flags 99, 147, 83, 163. Reads aligning to the *Drosophila* genome were counted for spike-in normalization. BigWig coverage tracks were then generated using deepTools. Normalization factors were derived by taking the minimum number of reads mapped to the spike-in genome across all samples and dividing that by the number of mapped spike-in reads for each sample.

S2 cell PRO-seq analysis was carried out as described (Elrod et al., 2019). Paired-end reads were trimmed to 40nt, for adaptor sequence and low quality 3' ends using cutadapt 1.14, discarding those containing reads shorter than 20nt (-m 20 -q 10), to allow successful alignment with Bowtie 1.2.2 (Langmead et al., 2009). Remaining pairs were paired-end aligned to the hg38 genome index to determine spike-normalization ratios based on uniquely mapped reads. Pairs mapping to hg38 were omitted from subsequent analysis, and unmapped pairs were aligned to the dm3 genome assembly. Identical parameters were used in each alignment described above: up to 2 mismatches, and unmappable pairs routed to separate output files (-v2, -un, --best). Pairs mapping to dm3, representing biotin-

labeled RNA 3’ ends, were separated, and strand-specific counts of the 3' mapping positions determined at single nucleotide resolution, genome-wide, and expressed in bedGraph format with “plus” and “minus” strand labels swapped for each 3' bedGraph, to correct for the “forward/reverse” nature of Illumina paired-end sequencing (Mahat et al., 2016). Based on similar recovery of spike-in reads, depth normalization was performed and bedGraphs from replicates of each condition were combined by summing counts per nucleotide.

Definition of mammalian TSSs

Candidate TSSs in MCF-7 cells were obtained from the public CAGE-seq dataset (FANTOM5) (Lizio et al., 2015) are filtered with our PRO-seq densities (TPM>1 at TSS 0-100 bp regions). Adjacent TSSs within 100bp are merged to keep the highest expressed TSS among them. Together we defined 11,936 mRNA TSSs (<100 bp to the annotated Refseq gene TSSs on the same strand) and 1,159 PROMPTs TSSs (<100 bp to the annotated Refseq gene TSSs on the opposite strand). We also defined 2,488 enhancer RNA TSSs (intergenic TSSs within the enhancer regions determined by public STARR-seq data in MCF-7 (ENCODE) (Davis et al., 2018; ENCODE Project Consortium, 2012).

***Drosophila* TSS list and clustering based on promoter Pol II decay rate**

Active TSS were defined using Start-Seq data in *Drosophila* S2 cells, published previously (Henriques et al., 2018) and available from GEO (GSE85191). Clusters of Pol II decay rates at active TSSs were based on half-lives of Start-RNAs as described in (Elrod et al., 2019).

Expression matching

The TSS list of all active *Drosophila* promoters was filtered for those with calculated decay rates (Henriques et al., 2018). Counts within 25 bp bins from the N=2 bedGraph were summed from -250 to +250 relative to the remaining 8,389 mRNA gene TSSs. These sums were used to rank by METTL3 binding and the top 500 were defined as the “High METTL3”

gene IDs. The IDs of the lower half (~4,195 TSSs) were then fed into a custom expression matching script (Deposited on Github: https://github.com/AdelmanLab/ExpressionMatch). For expression, PRO-seq read sums from TSS to +2kb were counted using the control PRO-seq N=3 bedGraphs. The resulting list of 500 gene IDs represent the bottom, expression matched METTL3 genes. Note: 2 outlier TSS (corresponding to two isoforms of the gene Gale) were removed from the PRO-seq metagene using the High 500 METTL3 targets.

Metagene analysis

Composite metagene distributions were generated by summing sequencing reads at each indicated position with respect to the TSS and dividing by the number of TSSs included within each group. These were plotted for a range in distances around the TSS. Heatmap of S2 cell METTL3 ChIP was generated using Partek Genomics Suite version 7.19.1125.

Analyses of repeats correlation

Correlation between sequencing sample repeats are calculated with deeptools. Briefly, coverage on every 10kb bins across genome are calculated with multiBigwigSummary, and pearson correlation test are carried out using plotCorrelation. Pearson correlation coefficients for the biological replicates are listed in Table S3.

Statistical Analysis

The statistical data are presented as mean ± SD, as described in the figure legends. The statistical significance of differences was determined using Student's t test. * $p < 0.05$, ** $p < 0.01$. For human and mouse ChIP-seq box plots, statistical significance was calculated and Paired t-test. For *Drosophila* ChIP-seq box plots, statistical significance was determined using Mann-Whitney pairwise tests. For *Drosophila* ChIP-seq correlation test, Spearman's correlation coefficient is shown.

Supplementary Table1: List of SiRNA Sequences

Supplementary Table2: List of DNA Oligonucleotides

Supplementary Table3: Pearson Correlation Coefficients for the Biological Replicates

References:

Akhtar, J., Renaud, Y., Albrecht, S., Ghavi-Helm, Y., Roignant, J.Y., Silies, M., and Junion, G. (2021). m6A RNA methylation regulates promoter- proximal pausing of RNA polymerase II. MOL CELL *81*, 3356-3367.

Akichika, S., Hirano, S., Shichino, Y., Suzuki, T., Nishimasu, H., Ishitani, R., Sugita, A., Hirose, Y., Iwasaki, S., and Nureki, O., *et al.* (2019). Cap-specific terminal N (6)-methylation of RNA by an RNA polymerase II-associated methyltransferase. SCIENCE *363*.

Barbieri, I., Tzelepis, K., Pandolfini, L., Shi, J., Millan-Zambrano, G., Robson, S.C., Aspris, D., Migliori, V., Bannister, A.J., and Han, N., *et al.* (2017). Promoter-bound METTL3 maintains myeloid leukaemia by m(6)A-dependent translation control. NATURE *552*, 126-131.

Chelmicki, T., Roger, E., Teissandier, A., Dura, M., Bonneville, L., Rucli, S., Dossin, F., Fouassier, C., Lameiras, S., and Bourc'His, D. (2021). m(6)A RNA methylation regulates the fate of endogenous retroviruses. NATURE *591*, 312-316.

Chen, S., Zhou, Y., Chen, Y., and Gu, J. (2018). fastp: an ultra-fast all-in-one FASTQ preprocessor. BIOINFORMATICS 34, i884-i890.

Core, L., and Adelman, K. (2019). Promoter-proximal pausing of RNA polymerase II: a nexus of gene regulation. Genes Dev 33, 960-982.

Davis, C.A., Hitz, B.C., Sloan, C.A., Chan, E.T., Davidson, J.M., Gabdank, I., Hilton, J.A., Jain, K., Baymuradov, U.K., and Narayanan, A.K., et al. (2018). The Encyclopedia of DNA elements (ENCODE): data portal update. NUCLEIC ACIDS RES 46, D794-D801.

Dominissini, D., Moshitch-Moshkovitz, S., Schwartz, S., Salmon-Divon, M., Ungar, L., Osenberg, S., Cesarkas, K., Jacob-Hirsch, J., Amariglio, N., and Kupiec, M., *et al.* (2012). Topology of the human and mouse m6A RNA methylomes revealed by m6A-seq. NATURE *485*, 201-206.

Elrod, N.D., Henriques, T., Huang, K.L., Tatomer, D.C., Wilusz, J.E., Wagner, E.J., and Adelman, K. (2019). The Integrator Complex Attenuates Promoter-Proximal Transcription at Protein-Coding Genes. MOL CELL *76*, 738-752.

ENCODE Project Consortium (2012). An integrated encyclopedia of DNA elements in the human genome. NATURE 489, 57-74.

Ezzeddine, N., Chen, J., Waltenspiel, B., Burch, B., Albrecht, T., Zhuo, M., Warren, W.D., Marzluff, W.F., and Wagner, E.J. (2011). A subset of Drosophila integrator proteins is essential for efficient U7 snRNA and spliceosomal snRNA 3'-end formation. MOL CELL BIOL 31, 328-341.

Gaidatzis, D., Burger, L., Florescu, M., and Stadler, M.B. (2015). Analysis of intronic and exonic reads in RNA-seq data characterizes transcriptional and post-transcriptional regulation. NAT BIOTECHNOL 33, 722-729.

Gates, L.A., Foulds, C.E., and O'Malley, B.W. (2017). Histone Marks in the 'Driver's Seat': Functional Roles in Steering the Transcription Cycle. TRENDS BIOCHEM SCI *42*, 977-989.

Henriques, T., Scruggs, B.S., Inouye, M.O., Muse, G.W., Williams, L.H., Burkholder, A.B., Lavender, C.A., Fargo, D.C., and Adelman, K. (2018). Widespread

transcriptional pausing and elongation control at enhancers. Genes Dev 32, 26-41.
Jia, G., Fu, Y., Zhao, X., Dai, Q., Zheng, G., Yang, Y., Yi, C., Lindahl, T., Pan, T., and Yang, Y.G., *et al.* (2011). N6-methyladenosine in nuclear RNA is a major substrate of the obesity-associated FTO. NAT CHEM BIOL *7*, 885-887.
Judd, J., Duarte, F.M., and Lis, J.T. (2021). Pioneer-like factor GAF cooperates with PBAP (SWI/SNF) and NURF (ISWI) to regulate transcription. Genes Dev 35, 147-156.
Kan, L., Ott, S., Joseph, B., Park, E.S., Dai, W., Kleiner, R.E., Claridge-Chang, A., and Lai, E.C. (2021). A neural m6A/Ythdf pathway is required for learning and memory in Drosophila. NAT COMMUN *12*, 1458.
Kaya-Okur, H.S., Wu, S.J., Codomo, C.A., Pledger, E.S., Bryson, T.D., Henikoff, J.G., Ahmad, K., and Henikoff, S. (2019). CUT&Tag for efficient epigenomic profiling of small samples and single cells. NAT COMMUN *10*, 1930.
Ke, S., Pandya-Jones, A., Saito, Y., Fak, J.J., Vagbo, C.B., Geula, S., Hanna, J.H., Black, D.L., Darnell, J.J., and Darnell, R.B. (2017). m(6)A mRNA modifications are deposited in nascent pre-mRNA and are not required for splicing but do specify cytoplasmic turnover. Genes Dev *31*, 990-1006.
Knuckles, P., Carl, S.H., Musheev, M., Niehrs, C., Wenger, A., and Buhler, M. (2017). RNA fate determination through cotranscriptional adenosine methylation and microprocessor binding. NAT STRUCT MOL BIOL *24*, 561-569.
Langmead, B., Trapnell, C., Pop, M., and Salzberg, S.L. (2009). Ultrafast and memory-efficient alignment of short DNA sequences to the human genome. GENOME BIOL 10, R25.
Lasman, L., Krupalnik, V., Viukov, S., Mor, N., Aguilera-Castrejon, A., Schneir, D., Bayerl, J., Mizrahi, O., Peles, S., and Tawil, S., *et al.* (2020). Context-dependent functional compensation between Ythdf m(6)A reader proteins. Genes Dev *34*, 1373-1391.
Lee, J.H., Wang, R., Xiong, F., Krakowiak, J., Liao, Z., Nguyen, P.T., Moroz-Omori, E.V., Shao, J., Zhu, X., and Bolt, M.J., *et al.* (2021). Enhancer RNA m6A methylation facilitates transcriptional condensate formation and gene activation. MOL CELL *81*, 3368-3385.
Li, H., Handsaker, B., Wysoker, A., Fennell, T., Ruan, J., Homer, N., Marth, G., Abecasis, G., and Durbin, R. (2009). The Sequence Alignment/Map format and SAMtools. BIOINFORMATICS 25, 2078-2079.
Liu, J., Dou, X., Chen, C., Chen, C., Liu, C., Xu, M.M., Zhao, S., Shen, B., Gao, Y., and Han, D., *et al.* (2020). N (6)-methyladenosine of chromosome-associated regulatory RNA regulates chromatin state and transcription. SCIENCE *367*, 580-586.
Liu, J., Gao, M., He, J., Wu, K., Lin, S., Jin, L., Chen, Y., Liu, H., Shi, J., and Wang, X., *et al.* (2021). The RNA m(6)A reader YTHDC1 silences retrotransposons and guards ES cell identity. NATURE *591*, 322-326.
Liu, N., Zhou, K.I., Parisien, M., Dai, Q., Diatchenko, L., and Pan, T. (2017). N6-methyladenosine alters RNA structure to regulate binding of a low-complexity protein. NUCLEIC ACIDS RES *45*, 6051-6063.
Lizio, M., Harshbarger, J., Shimoji, H., Severin, J., Kasukawa, T., Sahin, S., Abugessaisa, I., Fukuda, S., Hori, F., and Ishikawa-Kato, S., et al. (2015). Gateways to

the FANTOM5 promoter level mammalian expression atlas. GENOME BIOL 16, 22.
Louloupi, A., Ntini, E., Conrad, T., and Orom, U. (2018). Transient N-6-Methyladenosine Transcriptome Sequencing Reveals a Regulatory Role of m6A in Splicing Efficiency. CELL REP *23*, 3429-3437.
Loven, J., Hoke, H.A., Lin, C.Y., Lau, A., Orlando, D.A., Vakoc, C.R., Bradner, J.E., Lee, T.I., and Young, R.A. (2013). Selective inhibition of tumor oncogenes by disruption of super-enhancers. CELL 153, 320-334.
Lykke-Andersen, S., Zumer, K., Molska, E.S., Rouviere, J.O., Wu, G., Demel, C., Schwalb, B., Schmid, M., Cramer, P., and Jensen, T.H. (2021). Integrator is a genome-wide attenuator of non-productive transcription. MOL CELL *81*, 514-529.
Mahat, D.B., Kwak, H., Booth, G.T., Jonkers, I.H., Danko, C.G., Patel, R.K., Waters, C.T., Munson, K., Core, L.J., and Lis, J.T. (2016). Base-pair-resolution genome-wide mapping of active RNA polymerases using precision nuclear run-on (PRO-seq). NAT PROTOC 11, 1455-1476.
Meyer, K.D., Saletore, Y., Zumbo, P., Elemento, O., Mason, C.E., and Jaffrey, S.R. (2012). Comprehensive Analysis of mRNA Methylation Reveals Enrichment in 3 ' UTRs and near Stop Codons. CELL *149*, 1635-1646.
Ping, X.L., Sun, B.F., Wang, L., Xiao, W., Yang, X., Wang, W.J., Adhikari, S., Shi, Y., Lv, Y., and Chen, Y.S., *et al.* (2014). Mammalian WTAP is a regulatory subunit of the RNA N6-methyladenosine methyltransferase. CELL RES *24*, 177-189.
Quinlan, A.R., and Hall, I.M. (2010). BEDTools: a flexible suite of utilities for comparing genomic features. BIOINFORMATICS 26, 841-842.
Ramirez, F., Ryan, D.P., Gruning, B., Bhardwaj, V., Kilpert, F., Richter, A.S., Heyne, S., Dundar, F., and Manke, T. (2016). deepTools2: a next generation web server for deep-sequencing data analysis. NUCLEIC ACIDS RES 44, W160-W165.
Sendinc, E., Valle-Garcia, D., Dhall, A., Chen, H., Henriques, T., Navarrete-Perea, J., Sheng, W., Gygi, S.P., Adelman, K., and Shi, Y. (2019). PCIF1 Catalyzes m6Am mRNA Methylation to Regulate Gene Expression. MOL CELL 75, 620-630.
Shi, H., Wei, J., and He, C. (2019). Where, When, and How: Context-Dependent Functions of RNA Methylation Writers, Readers, and Erasers. MOL CELL *74*, 640-650.
Sledz, P., and Jinek, M. (2016). Structural insights into the molecular mechanism of the m(6)A writer complex. ELIFE *5*.
Trapnell, C., Pachter, L., and Salzberg, S.L. (2009). TopHat: discovering splice junctions with RNA-Seq. BIOINFORMATICS 25, 1105-1111.
Wang, P., Doxtader, K.A., and Nam, Y. (2016). Structural Basis for Cooperative Function of Mettl3 and Mettl14 Methyltransferases. MOL CELL *63*, 306-317.
Wang, X., Feng, J., Xue, Y., Guan, Z., Zhang, D., Liu, Z., Gong, Z., Wang, Q., Huang, J., and Tang, C., *et al.* (2016). Structural basis of N(6)-adenosine methylation by the METTL3-METTL14 complex. NATURE *534*, 575-578.
Wang, Y., Zhang, L., Ren, H., Ma, L., Guo, J., Mao, D., Lu, Z., Lu, L., and Yan, D. (2021). Role of Hakai in m6A modification pathway in Drosophila. NAT COMMUN *12*, 2159.
Xiang, Y., Laurent, B., Hsu, C.H., Nachtergaele, S., Lu, Z., Sheng, W., Xu, C., Chen,

H., Ouyang, J., and Wang, S., *et al.* (2017). RNA m(6)A methylation regulates the ultraviolet-induced DNA damage response. NATURE *543*, 573-576.
Xiao, S., Cao, S., Huang, Q., Xia, L., Deng, M., Yang, M., Jia, G., Liu, X., Shi, J., and Wang, W., *et al.* (2019). The RNA N(6)-methyladenosine modification landscape of human fetal tissues. NAT CELL BIOL *21*, 651-661.
Xu, W., Li, J., He, C., Wen, J., Ma, H., Rong, B., Diao, J., Wang, L., Wang, J., and Wu, F., *et al.* (2021). METTL3 regulates heterochromatin in mouse embryonic stem cells. NATURE *591*, 317-321.
Yu, G., Wang, L.G., and He, Q.Y. (2015). ChIPseeker: an R/Bioconductor package for ChIP peak annotation, comparison and visualization. BIOINFORMATICS 31, 2382-2383.
Zaccara, S., and Jaffrey, S.R. (2020). A Unified Model for the Function of YTHDF Proteins in Regulating m(6)A-Modified mRNA. CELL *181*, 1582-1595.
Zheng, G., Dahl, J.A., Niu, Y., Fedorcsak, P., Huang, C.M., Li, C.J., Vagbo, C.B., Shi, Y., Wang, W.L., and Song, S.H., *et al.* (2013). ALKBH5 is a mammalian RNA demethylase that impacts RNA metabolism and mouse fertility. MOL CELL *49*, 18-29.
Zhou, K.I., Shi, H., Lyu, R., Wylder, A.C., Matuszek, Z., Pan, J.N., He, C., Parisien, M., and Pan, T. (2019). Regulation of Co-transcriptional Pre-mRNA Splicing by m(6)A through the Low-Complexity Protein hnRNPG. MOL CELL *76*, 70-81.

KEY RESOURCES TABLE

REAGENT or RESOURCE	SOURCE	IDENTIFIER
Antibodies		
METTL3	Bethyl	Cat#A301-567A
METTL14	Sigma	Cat#HPA038002
WTAP	Bethyl	Cat#A301-435A
WTAP	Proteintech	Cat#10200-1-AP
ALKBH5	Abcam	Cat#ab69325
INTS11	Bethyl	Cat#A301-274A
hnRNP G	Cell Signaling	Cat#14794S
H3K4me3	Cell Signaling	Cat#9751S
H3K4me1	Active Motif	Cat#39297
H3K27Ac	Millipore	Cat#07-360
HA-Tag	Cell Signaling	Cat#3724S
m^6A	Synaptic Systems	Cat#202003
YTHDC1	Cell Signaling	Cat#77422
YTHDF2	Proteintech	Cat#24744-1-AP
Lamin B1	Proteintech	Cat#66095-1-Ig
Tubulin	Proteintech	Cat#66031-1-Ig
Actin	Proteintech	Cat#60008-1-Ig
GAPDH	Proteintech	Cat#60004-1-Ig
Normal rabbit IgG	Santa Cruz	Cat#sc-2027
Ints9	(Ezzeddine et al., 2011)	/
Hitone H3	Abcam	Cat#ab1791
Chemicals, Peptides, and Recombinant Proteins		
Protease Inhibitor Cocktail	Roche	Cat#4693159001
Lipofectamine 2000	Invitrogen	Cat#11668019
Lipofectamine RNAiMAX	Invitrogen	Cat#13778150
TRIzol reagent	Invitrogen	Cat#15596018
Dynabeads MyOne Streptavidin T1 beads	Invitrogen	Cat#65601
Dynabeads Protein A/Protein G	Invitrogen	Cat#10015D
RNase A, DNase and protease-free	Thermo	Cat#EN0531
Proteinase K	New England Biolabs	Cat# P8107S
Biotin-11-NTPs	Perkin Elmer	Cat# NEL54(2/3/4/5)001
Proteinase K	New England Biolabs	Cat# P8107S
Critical Commercial Assays		
MinElute PCR Purification Kit	Qiagen	Cat#28006
FastStart Universal SYBR Green Master (Rox)	Roche	Cat#4913914001
TURBO DNA-free Kit	Invitrogen	Cat#AM1970
PrimeScript RT reagent kit	Takara	Cat#RR047A
ACCEL-NGS 2S PLUS DNA LibraryKit	SWIFT	Cat#21096
VAHTS Universal Plus DNA Library Prep Kit for Illumina	Vazyme	Cat#ND617
HyperactiveTM In-Situ ChIP Library Prep Kit for Illumina	Vazyme	Cat#TD901
Deposited Data		
Raw and analyzed data	This paper	GEO: GSE144404, GSE186784

MCF-7 STARR	(Davis et al., 2018; ENCODE Project Consortium, 2012)	ENCODE: ENCFF344TJT, ENCFF070QGP
Start-Seq	(Henriques et al., 2018)	GEO: GSE85191
IntS1 ChIP-seq in DL1	(Elrod et al., 2019)	GEO: GSE114467
Experimental Models: Cell Lines		
MCF-7	ATCC	N/A
HEK293T	ATCC	N/A
Mouse Neural Stem cells (mNSCs)	Laboratory of Jian Hu	N/A
S2-DGRC clone 6	DGRC	Stock number 6
Oligonucleotides		
SiRNA sequences	This paper	See Table S1
Primers for qPCR	This paper	See Table S2
Recombinant DNA		
Plasmid: PMSCV-Flag/HA-*METTL3*	This paper	N/A
Plasmid: PMSCV-Flag/HA-*METTL14*	This paper	N/A
Plasmid: PMSCV-Flag/HA-*WTAP*	This paper	N/A
Plasmid: PMSCV-Flag/HA-*ALKBH5*	This paper	N/A
Software and Algorithms		
Tophat2	(Trapnell et al., 2009)	https://ccb.jhu.edu/software/tophat/index.shtml
Bowtie	(Langmead et al., 2009)	http://bowtie-bio.sourceforge.net/index.shtm
Samtool	(Li et al., 2009)	http://www.htslib.org/doc/samtools.html
Bedtools	(Quinlan and Hall, 2010)	http://bedtools.readthedocs.io/en/latest
Deeptools	(Ramirez et al., 2016)	https://deeptools.readthedocs.io/en/develop/
Other		

Figure

Figure 1: The m^{6}A MTC components bind promoters and enhancers in MCF-7 cells

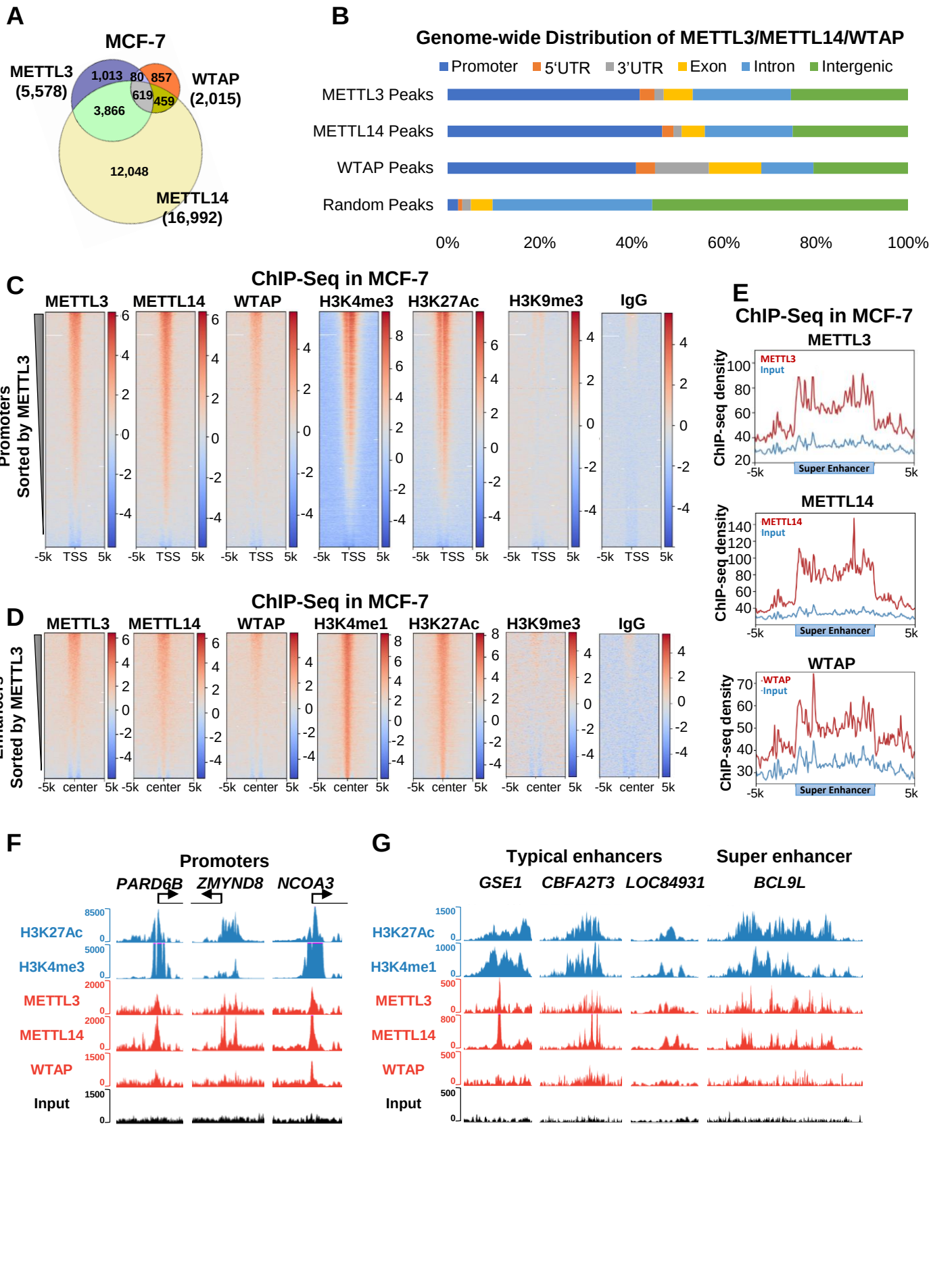

Figure 2: The m^{6}A MTC catalyzes m^{6}A in PROMPTs and eRNAs

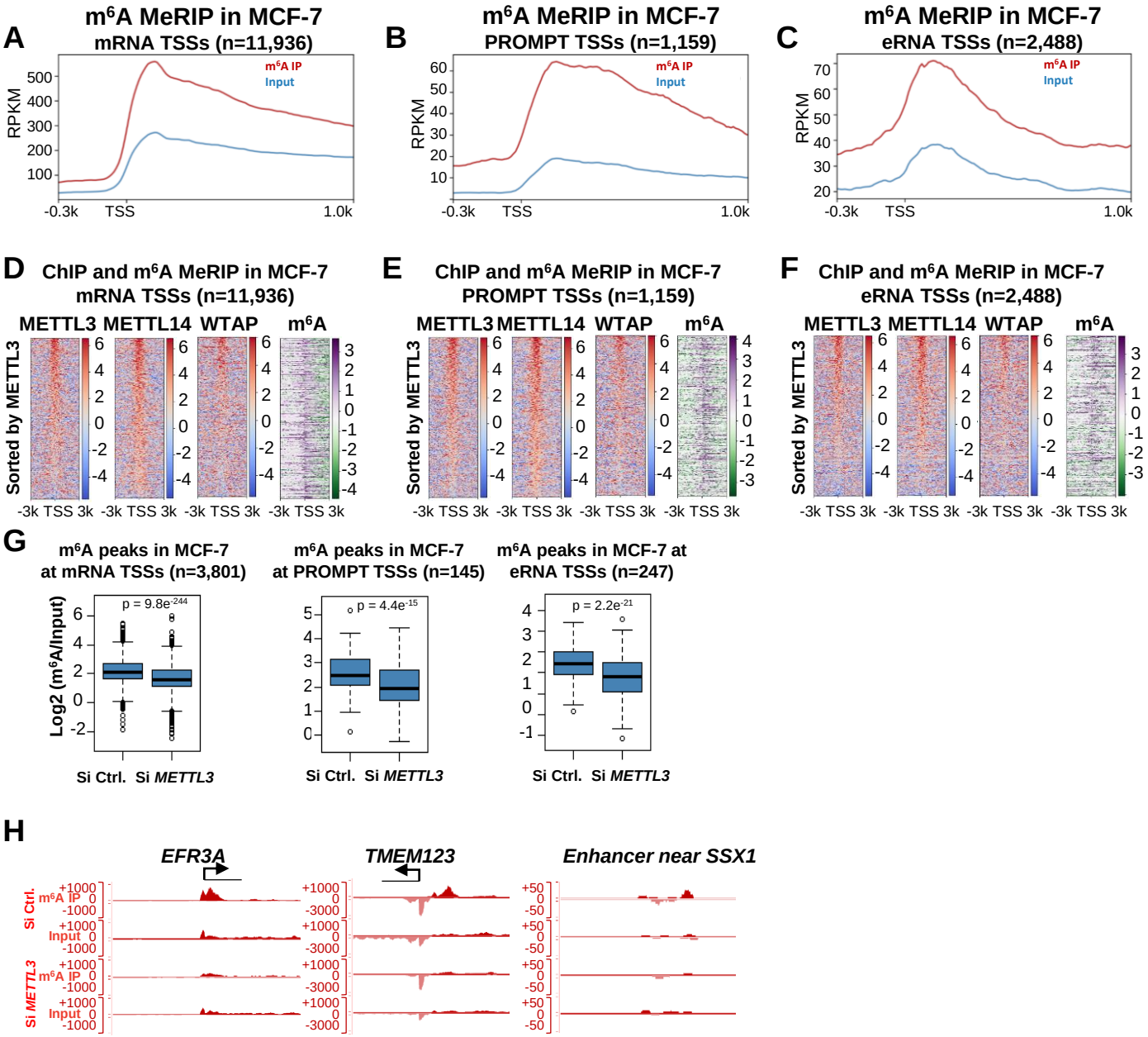

Figure 3: The m^{6}A MTC regulates nascent RNA biogenesis.

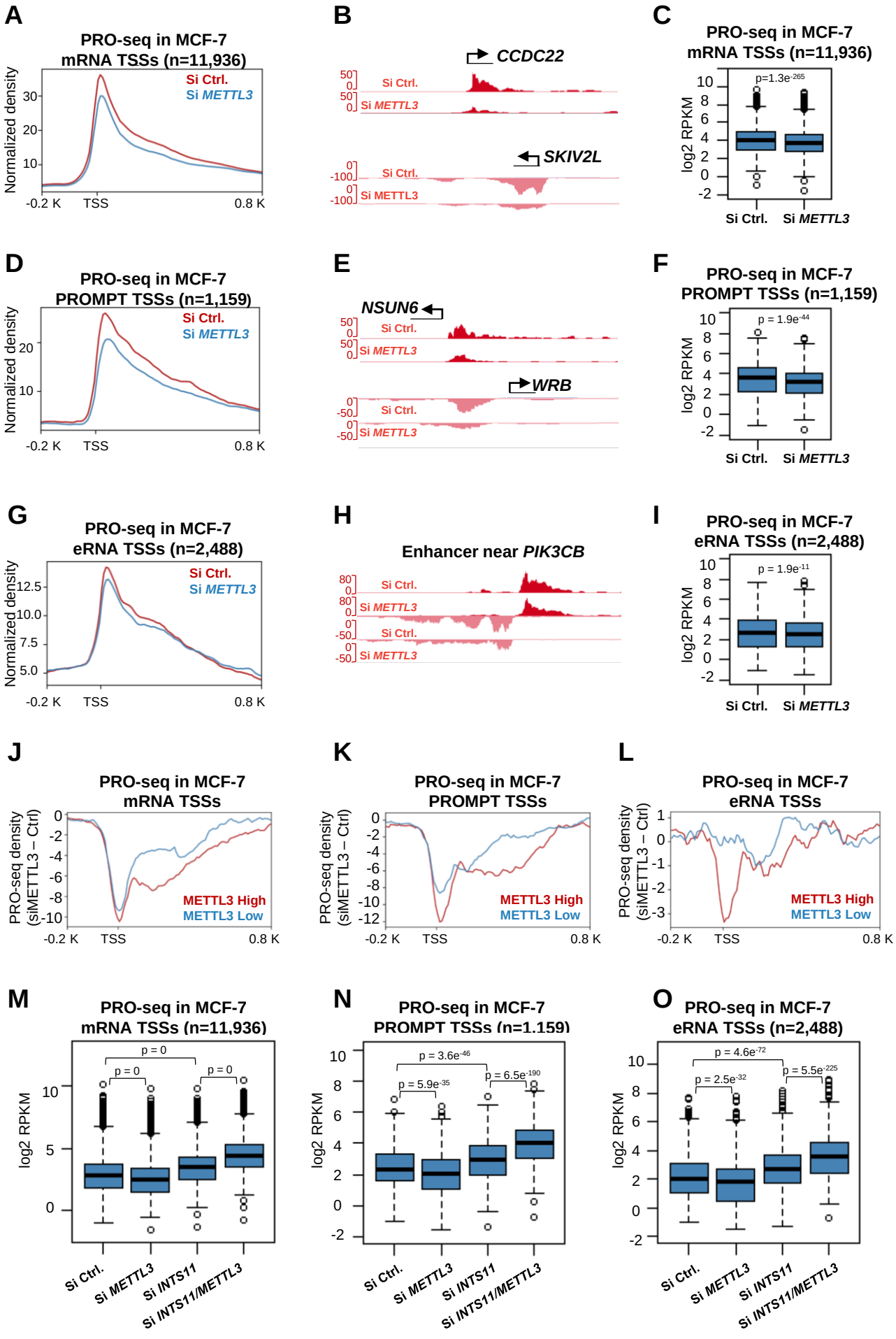

Figure 4: Nascent RNAs on promoters and enhancers are dynamically regulated by m^{6}A demethylase ALKBH5 in MCF-7 cells

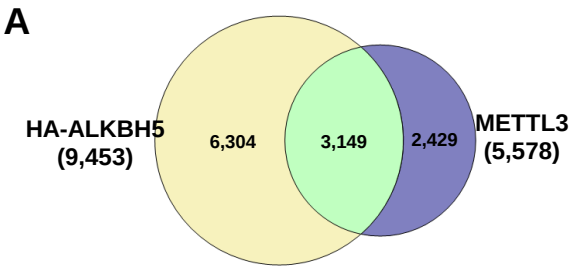

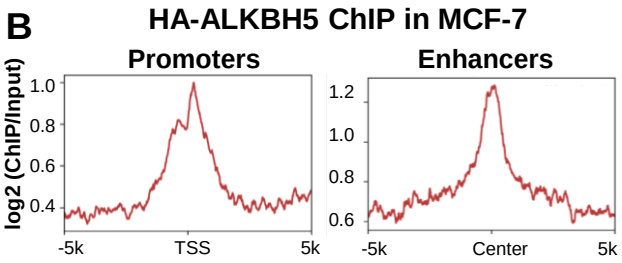

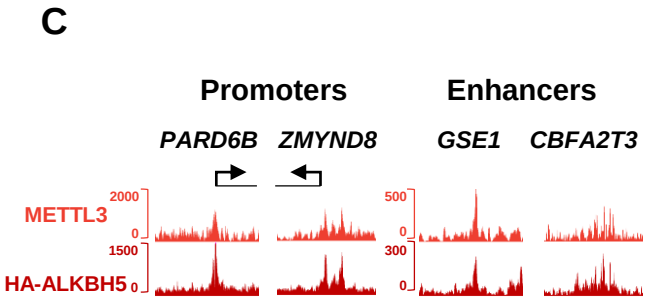

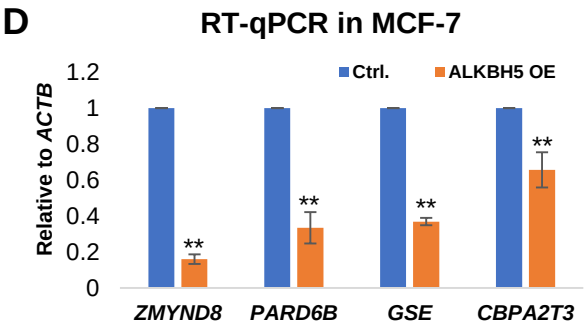

Figure 5: Loss of m^{6}A promotes INTS11 recruitment, which mediates nascent RNA cleavage in MCF-7 cells

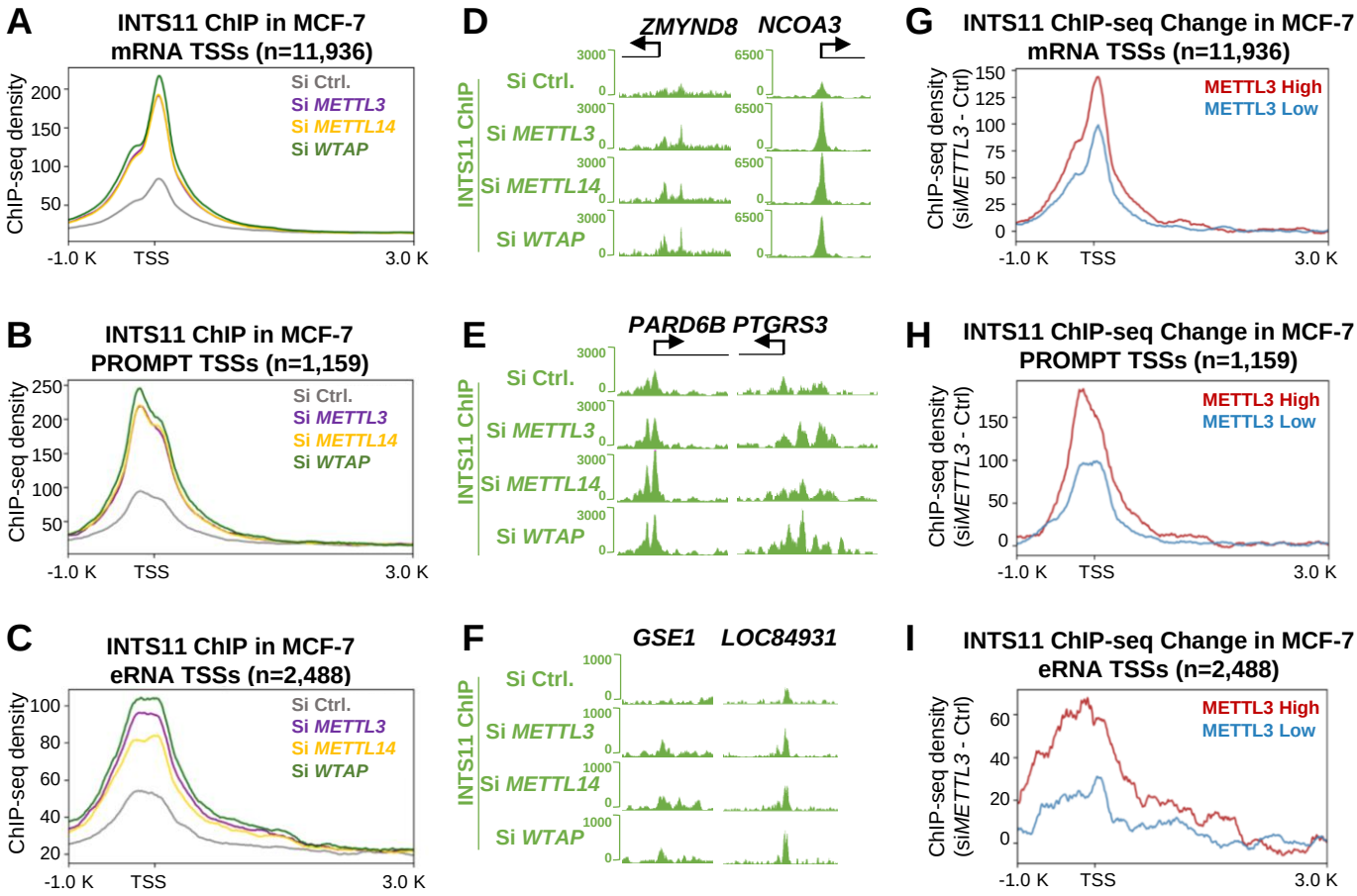

Figure 6: METTL3 and Integrator bind to different sets of genes in *Drosophila*

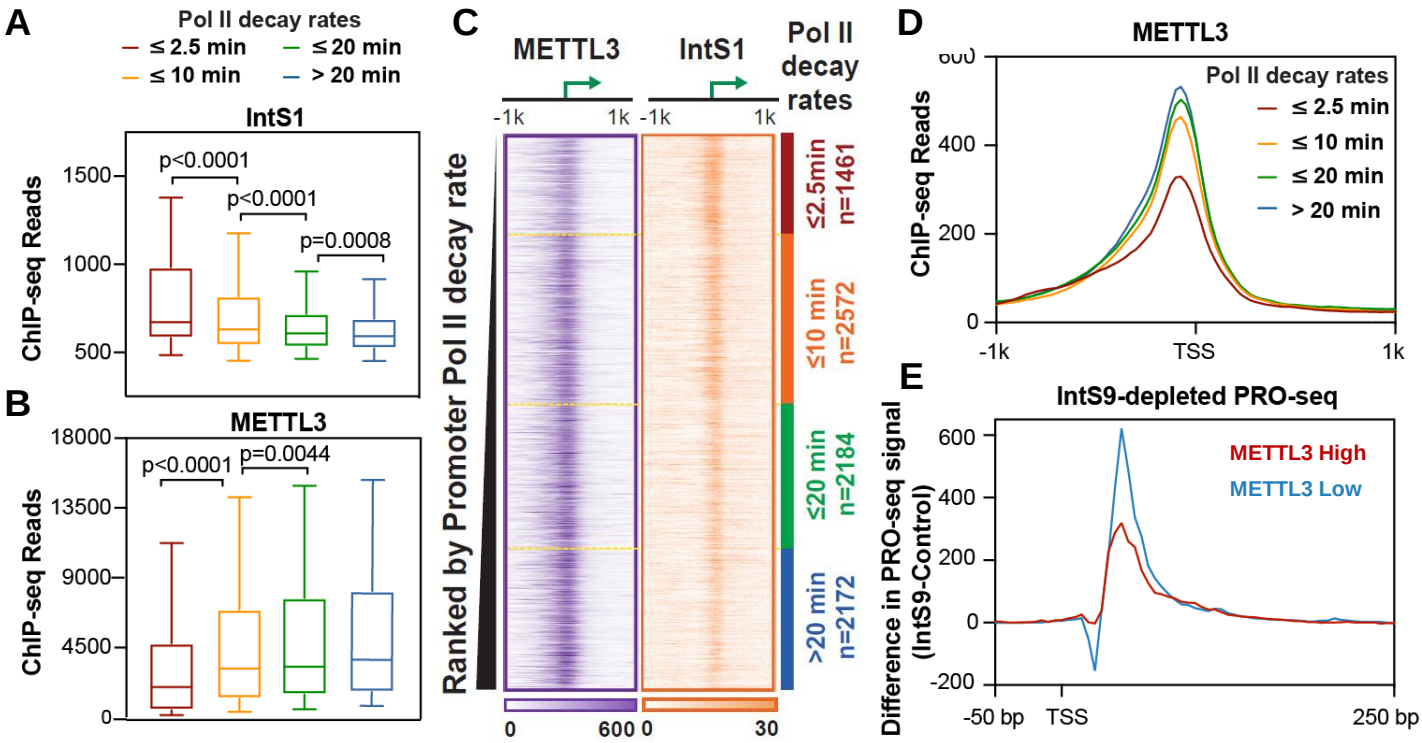

Figure 7: m^{6}A protects nascent RNAs from INST11-mediated cleavage through hnRNP G

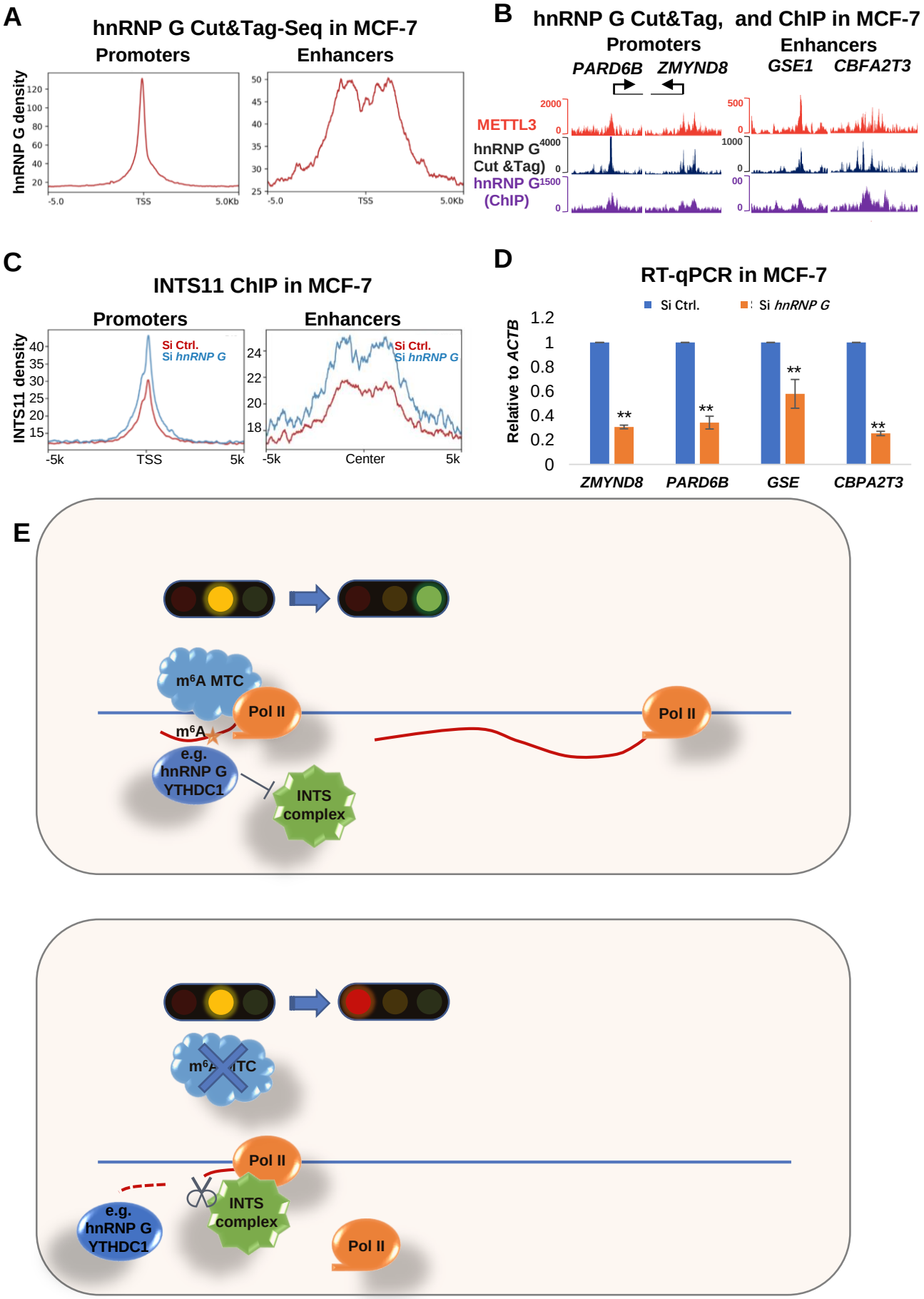

Figure S1. Related to Figure 1

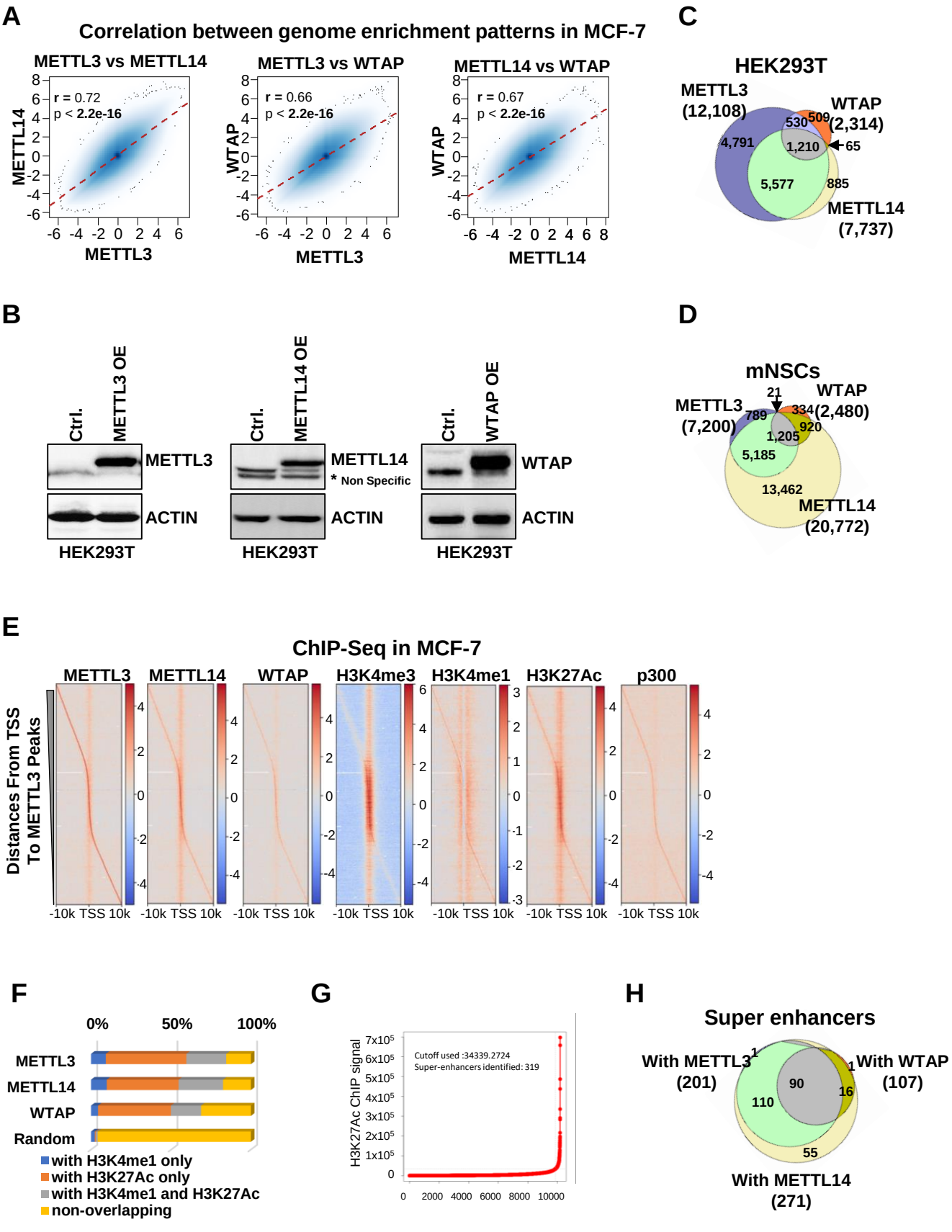

Figure S2: Related to Figure 1

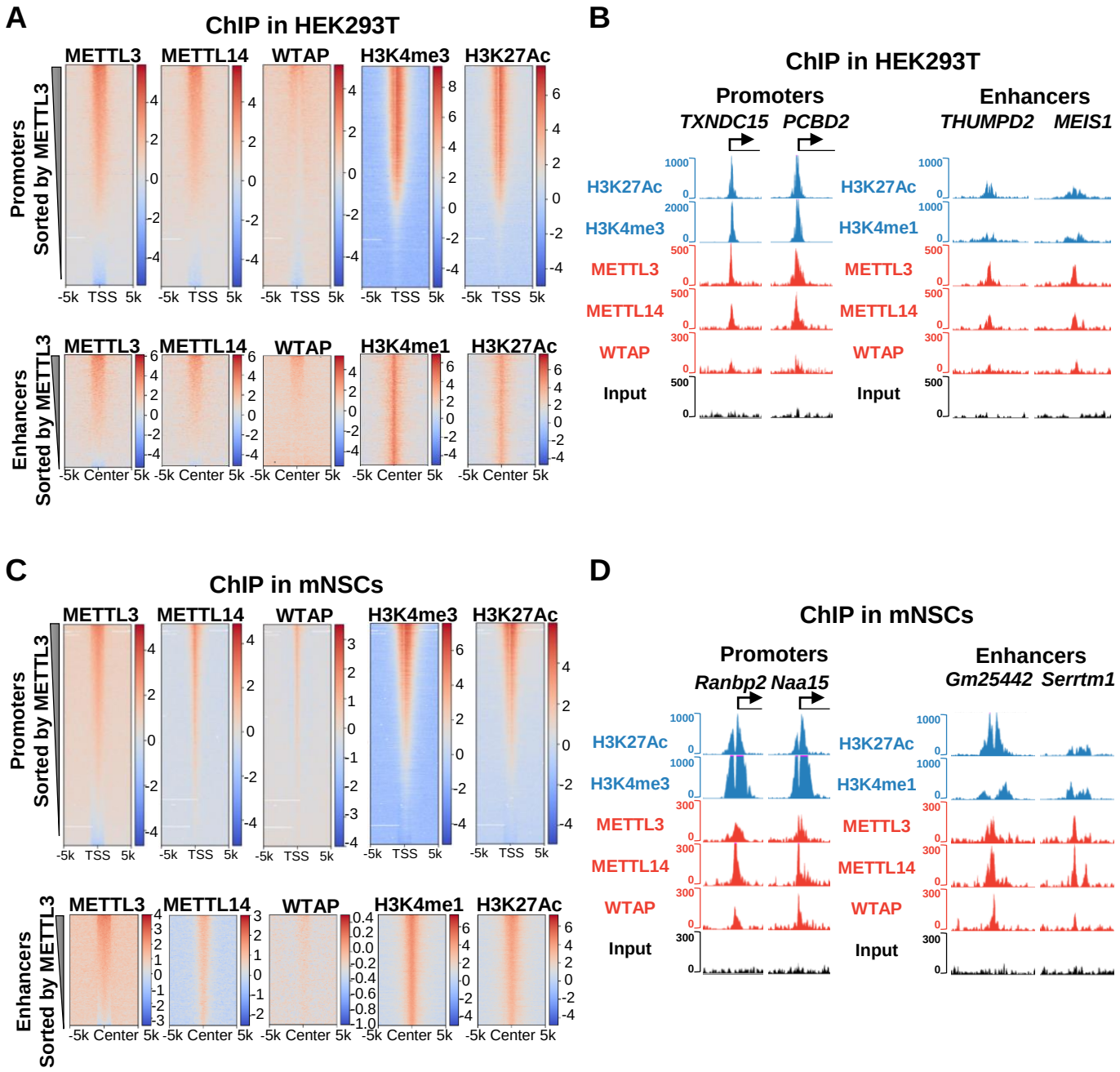

Figure S3: Related to Figures 2 - 3

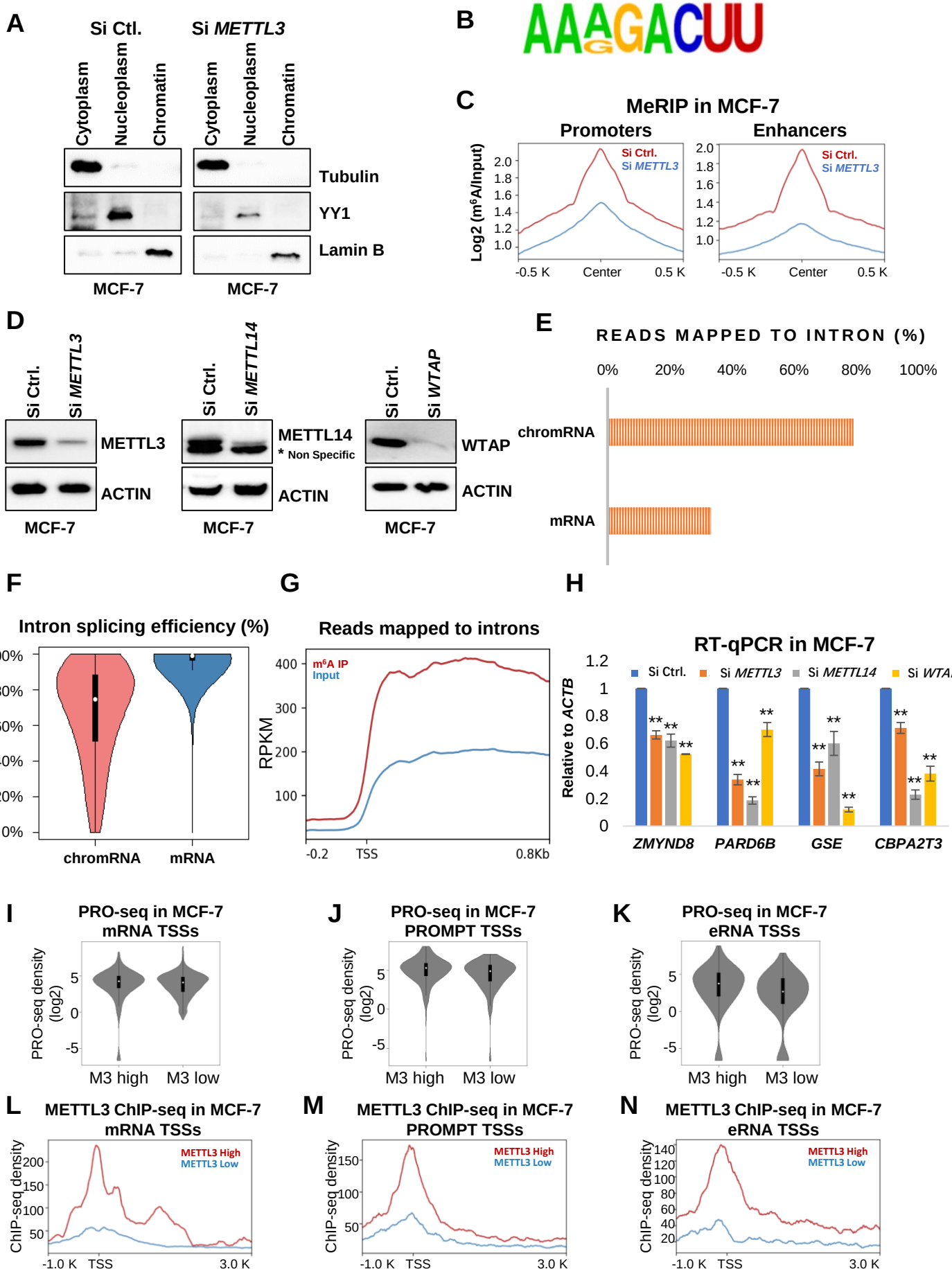

Figure S4: Related to Figures 3 - 5

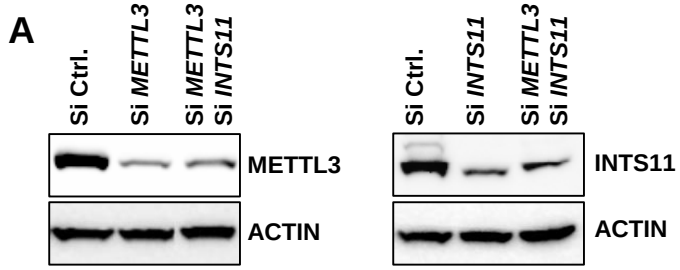

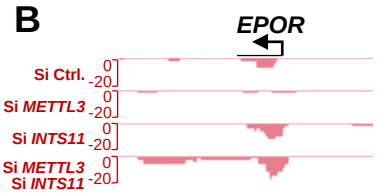

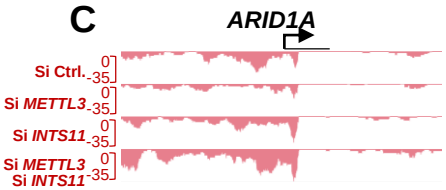

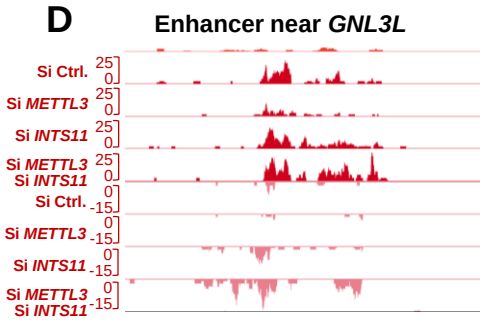

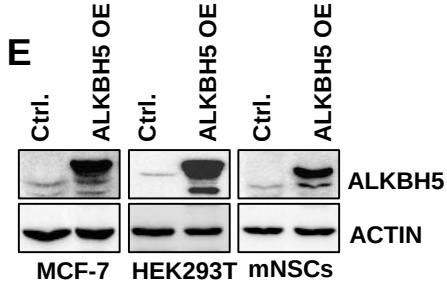

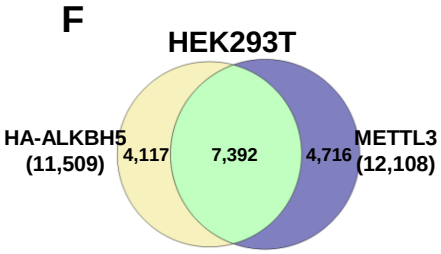

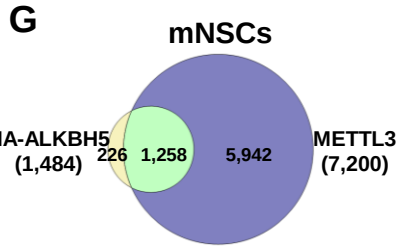

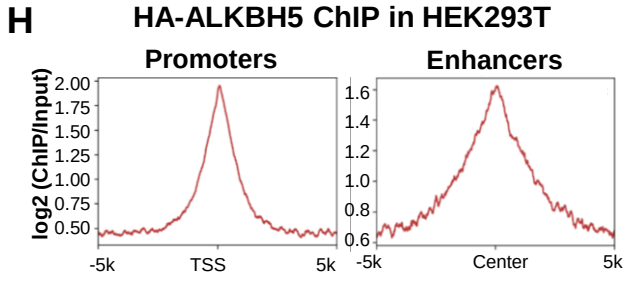

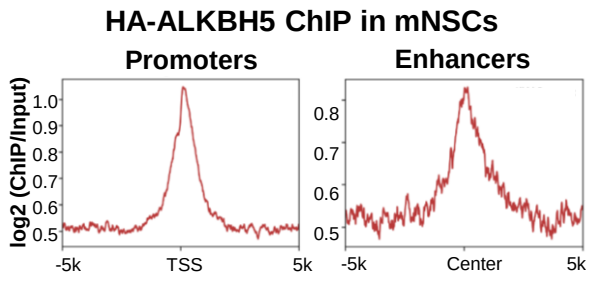

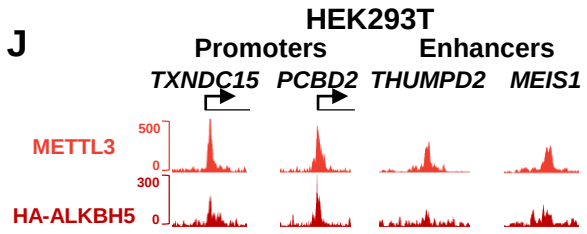

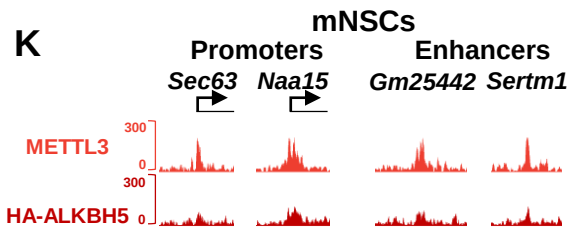

Figure S5: Related to Figures 6 - 7

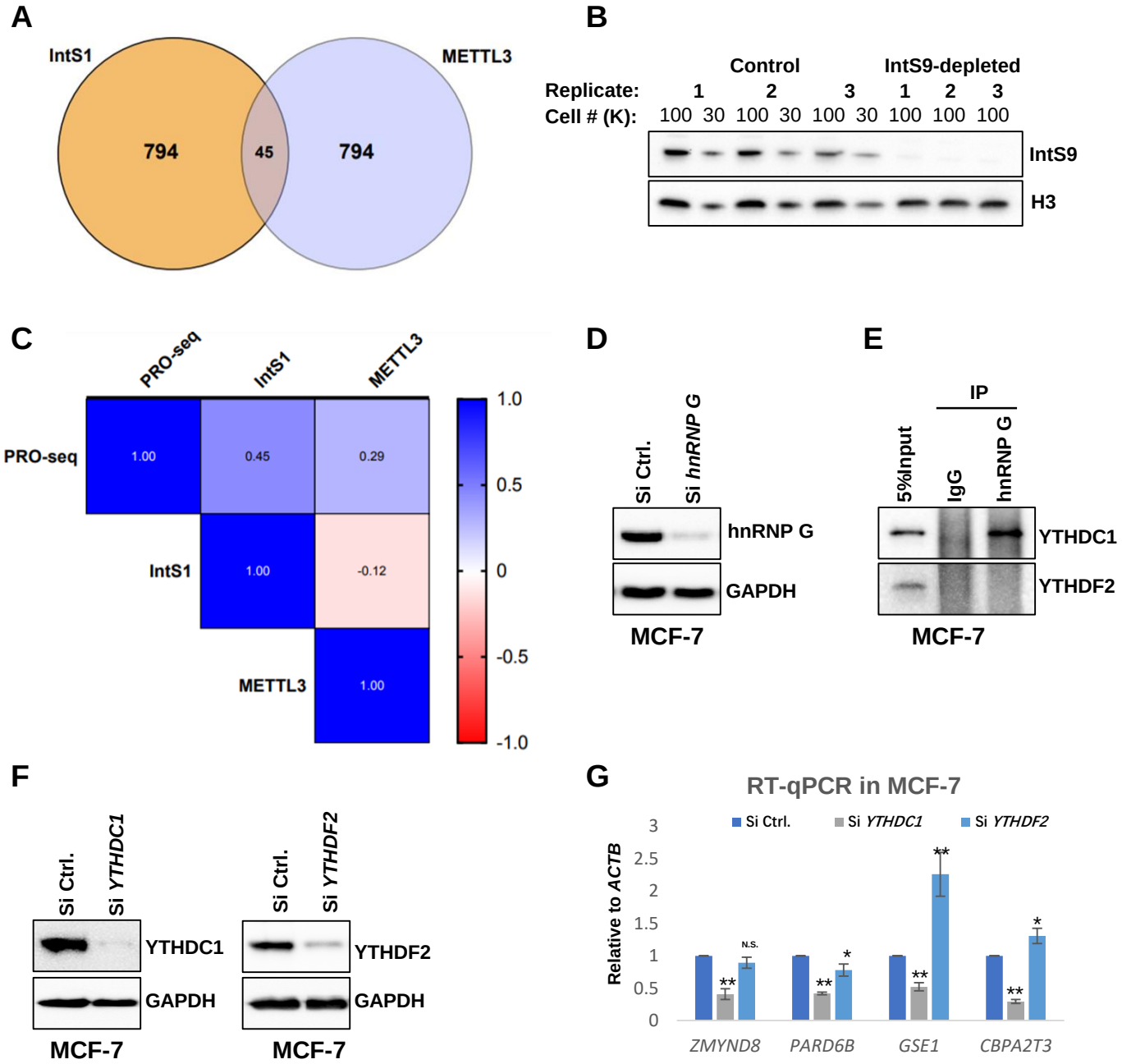

Figure S1: Related to Figure 1

A. Scatter plots showing positive correlations among binding patterns of METTL3, METTL14 and WTAP.

B. Western blots showing overexpression of METTL3 (Left), METTL14 (Middle), WTAP (Right) in HEK293T cells. * Non Specific band.

C-D. Venn diagram showing overlap of ChIP-seq peaks of METTL3, METTL14 and WTAP in HEK293T cells (C) and mouse neural stem cells (D).

E. Heatmaps showing enrichment levels (ChIP relative to Input) of METTL3, METTL14, WTAP and different histone modifications (H3K4me3, H3K4me1, H3K27Ac, and p300) around TSS in MCF-7 cells. Heatmaps were ranked by distances from TSS to METTL3 peaks.

F. Bar plots showing proportions of METTL3, METTL14 and WTAP peaks overlapping with H3K4me1 and H3K27Ac marks with random peaks as control in MCF-7 cells.

G. Points plot showing super enhancers determined by ROSE algorism in MCF-7 cells.

H. Venn diagram showing overlap of super enhancers bound by METTL3, METTL14 and WTAP in MCF-7 cells.

For ChIP-seq, representative of two biological replicates were shown. Pearson correlation coefficients for the biological replicates are listed in Table S3. For blots, representative of two independent replicates were shown.

Figure S2: Related to Figure 1

A. Heatmaps showing the enrichment levels (ChIP relative to Input) of METTL3, METTL14, WTAP and different histone modifications (H3K27Ac and H3K4me3 or H3K4me1) over promoters (Top) and enhancers (Bottom) in HEK293T cells. Heatmaps were ranked by METTL3 enrichment.

B. Snapshots of UCSC genome browser showing METTL3, METTL14 and WTAP binding events at representative promoters and representative enhancers in HEK293T cells.

C. Heatmaps showing the enrichment levels (ChIP relative to Input) of METTL3, METTL14, WTAP and different histone modifications (H3K27Ac and H3K4me3 or H3K4me1) over promoters (Top) and enhancers (Bottom) in mouse neural stem cells. Heatmaps were ranked by METTL3 enrichment.

D. Snapshots of UCSC genome browser showing METTL3, METTL14 and WTAP binding events at representative promoters and representative enhancers in mouse neural stem cells.

For ChIP-seq, representative of two biological replicates were shown.
Pearson correlation coefficients for the biological replicates are listed in Table S3.

Figure S3: Related to Figures 2 - 3

A. Western blots showing segregation of cytoplasmic Tubulin, nucleoplasmic YY1, and chromatin-associated Lamin B in MCF-7 cells.

B. Consensus motifs of promoter m^6A peaks and enhancer m^6A peaks in MCF-7 cells.

C. Aggregation plots showing decrease in m^6A enrichment over promoters (Left) and enhancers (Right) upon KD of METTL3 in MCF-7 cells.

D. Western blots showing KD efficiencies of METTL3, METTL14 and WTAP siRNAs in MCF-7 cells. * Non Specific band.

E. Chromatin associated RNAs have more sequencing reads mapped to introns than poly A RNAs.

F. Chromatin associated RNAs show significantly lower intron splicing efficiency than polyA RNAs.

G. Reads mapped to introns show significant m^6A enrichment in pre-mRNAs.

H. RT-qPCR assays showing decrease in nascent RNA level upon METTL3, METTL14 and WTAP KD at two representative promoters and two representative enhancers in MCF-7 cells.

I-K. Violin plots showing PRO-seq densities over high or low METTL3 bound gene TSSs (n=500) (I), PROMPT TSSs (n=200) (J), eRNA TSSs (n=200) (K) in MCF-7 cells.

L-N. Aggregation plots showing METTL3 binding levels over high or low METTL3 bound gene TSSs (n=500) (L), PROMPT TSSs (n=200) (M), eRNA TSSs (n=200) (N) in MCF-7 cells.

For ChIP-seq and PRO-seq, representative of two biological replicates were shown. Pearson correlation coefficients for the biological replicates are listed in Table S3. For blots, representative of two biological replicates were shown.

Figure S4: Related to Figures 3 - 5

A. Western blots showing KD efficiencies of METTL3 and INTS11 siRNAs in MCF-7 cells.

B-D. UCSC snapshots of representative regions of PRO-seq densities at TSSs of mRNA (M), PROMPT (N) and eRNA (O) in control, METTL3 KD, INTS11 KD and METTL3/INTS11 dual KD cells.

E. Western blots showing overexpression of HA-ALKBH5 in MCF-7 cells (Left), HEK293T cells (Middle) and mouse neural stem cells (Right).

F-G. Venn diagram showing overlap of ChIP-seq peaks between HA-ALKBH5 and METTL3 in HEK293T cells (F), and mouse neural stem cells (G).

H-I. Aggregation plots showing the HA-ALKBH5 binding levels over METTL3 bound promoters (Left) and enhancers (Right) in HEK293T cells (H), and mouse neural stem cells (I).

J-K. Snapshots of UCSC genome browser showing METTL3 and HA-ALKBH5 binding at two representative promoters and two representative enhancers in HEK293T cells (J), and mouse neural stem cells (K). For ChIP-seq, representative of two biological replicates were shown. Pearson correlation coefficients for the biological replicates are listed in Table S3.

Figure S5: Related to Figures 6 - 7

A. Venn diagram showing the overlap of METTL3 highly bound genes (top 10%, n=839) and IntS1 highly bound genes (top 10%, n=839).

B. Western blot for IntS9 (top) or Histone H3 (bottom) to assess IntS9-depletion after 3 days of dsRNA treatment. The three replicates corresponding to the S2 cell PRO-seq samples are included. A dilution of control protein extracted from 100K vs 30K cells facilitate quantification of knockdown efficiency.

C. Heatmap showing the correlation coefficient (Spearmans r) between the PRO-seq signal and ChIP-seq signal of IntS1 and METTL3 at active promoters (n=8,389). METTL3 and IntS1 ChIP-seq signals were summed from TSS +/- 250bp), and PRO-signal signal was summed from TSS to +150nt.

D. Western blots showing KD efficiencies of hnRNP G siRNAs in MCF-7 cells.

E. Western blots showing interaction of hnRNP G and YTHDC1, not YTHDF2.

F. Western blots showing KD efficiencies of YTHDC1 and YTHDF2 siRNAs in MCF-7 cells.

G. RT-qPCR assays showing decrease in nascent RNA level upon YTHDC1, but not YTHDF2 KD at two representative promoters and two representative enhancers in MCF-7 cells.

For RT-qPCR, all data are represented as mean ± SD from three biological repeats; ** p-value<0.01; t-test. For blots, representative of two independent replicates were shown.